Pure Appl. Chem., Vol. 78, No. 9, pp. 1619–1650, 2006.
doi:10.1351/pac200678091619

Soft chemical approaches to inorganic nanostructures*

C. N. R. Rao[1,2,‡], Ved Varun Agrawal[1], Kanishka Biswas[1,2], Ujjal K. Gautam[1,2], Moumita Ghosh[1,2], A. Govindaraj[1,2], G. U. Kulkarni[1], K. P. Kalyanikutty[1], Kripasindhu Sardar[1,2], and S. R. C. Vivekchand[1]

[1]Chemistry and Physics of Materials Unit and CSIR Centre of Excellence in Chemistry, Jawaharlal Nehru Centre for Advanced Scientific Research, Jakkur P.O., Bangalore 540064, India; [2]Solid State and Structural Chemistry Unit, Indian Institute of Science, Bangalore 560012, India

Abstract: Chemical approaches have emerged as the preferred means to synthesize nanostructures of various inorganic materials due to superior control over size, shape, and surface functionality. This article provides an overview of the contributions made in the authors' laboratory toward the synthesis of nanocrystals, nanowires, nanotubes, nanowalls, and other nanostructures of several inorganic materials. Thus, thiolized monodisperse metal nanocrystals have been obtained by a ligand exchange process and the stability of their 2D assemblies studied. Nanocrystals of pure CoO and ReO_3 have been synthesized, for the first time, employing a one-pot solvothermal technique. The solvothermal method has also been used to obtain organic soluble nanocrystals of semiconducting materials such as CdS, CdSe, and GaN. Inorganic nanowires and nanotubes have been prepared by several soft chemical routes, including surfactant-assisted synthesis and hydrogel templating. A simple reaction between elemental Se and Te with $NaBH_4$ in water has been utilized to obtain nanowires of Se and Te. We also describe the nebulized spray pyrolysis (NSP) technique to synthesize carbon nanotubes and nanowires of metals and III-V nitride semiconductors with improved yields. An important new technique for preparing nanocrystalline films of materials is by the reaction of the metal precursors in the organic layer at the interface of two immiscible liquids, with appropriate reagents. Nanocrystalline films of metals, alloys, and semiconductors and ultra-thin single-crystalline films of metal chalcogenides and oxides have been obtained by this technique. Apart from these, we discuss single precursor routes to iron sulfide, $GeSe_2$, and III-V nitride nanostructures as well as the first synthesis of GaS and GaSe nanowalls and nanotubes obtained through exfoliation by laser irradiation and thermal treatment.

Keywords: soft chemical routes; nanostructures; single-source precursors; liquid–liquid interface; solvothermal synthesis; nebulized spray pyrolysis.

*Paper based on a presentation at the 3rd IUPAC Workshop on Advanced Materials (WAM III), Stellenbosch, South Africa, 5–9 September 2005. Other presentations are published in this issue, pp. 1619–1801.

‡Corresponding author: Fax: (+91) 80 2362 2760; E-mail: cnrrao@jncasr.ac.in

INTRODUCTION

The important classes of nanomaterials are 0D nanocrystals, 1D nanowires and nanotubes, and 2D nanofilms and nanowalls. Nanocrystals and nanowires of a variety of materials have been recently synthesized and characterized [1–4]. Several inorganic nanotubes have also been synthesized and characterized [4,5]. Several of these materials have been obtained by methods such as evaporation of metals in an appropriate atmosphere, laser ablation, chemical vapor deposition (CVD), and carbon-assisted synthesis. These methods generally employ fairly high temperatures and drastic conditions. It has been, therefore, found necessary to explore methods which employ milder conditions and yet yield crystalline products with the desired size, shape, and other characteristics. In this context, there has been considerable success in the synthesis of nanocrystals, nanowires and nanotubes by chemical methods, especially those employing soft chemical routes. In this article, we describe the results of some of the efforts made in this laboratory to prepare nanocrystals, nanowires, and nanotubes by soft chemical methods. Typical of these methods are solvothermal synthesis, surfactant assistant synthesis, nebulized spray pyrolysis (NSP), and the use of hydrogels and liquid–liquid interfaces. We also include the essential characterization data on these materials by various techniques.

Thin films are well-known examples of 2D materials. The films are deposited on solid substrates by physical methods such as rf sputtering and pulse laser deposition [6]. We have explored a simple and new method involving the organic-aqueous interface, wherein a metal precursor in the organic layer reacts at the interface with an appropriate reagent present in the aqueous layer. This method has afforded ultra-thin films of metals, metal oxides and chalcogenides, many of which are single-crystalline. We also discuss the synthesis of GaS and GaSe nanowalls, which are two unique examples of 2D materials apart from the carbon nanowalls [7].

NANOCRYSTALS

Metal nanocrystals

Metal nanocrystals are generally prepared by the chemical reduction of metal salts. In order to prevent agglomeration, the nanocrystals are coated with capping agents such as surfactants and thiols [1–3,8]. Organic derivatized metal nanocrystals provide several advantages such as the possibility of size-selective precipitation, recrystallization, and formation of superlattice assemblies. Following the early work of Brust and coworkers [9], the general practice employed to obtain organic-capped metal nanocrystals is to use a biphasic mixture of an organic solvent and the aqueous solution of the metal salt in the presence of a phase-transfer reagent. The metal ion is transferred across the organic–water interface by the phase-transfer reagent and subsequently reduced in the presence of capping agents to yield sols of the metal nanocrystals. A novel technique developed in this laboratory involves the preparation of the metal nanocrystals in the aqueous phase followed by their transfer to a nonaqueous medium containing thiol molecules to yield an organosol [10,11]. In a typical preparation, a hydrosol containing small clusters of Au was prepared by the reduction of chloroaurate ions using partially hydrolyzed tetrakis(hydroxymethyl) phosphonium chloride. The Au nanocrystals so obtained in the aqueous phase was transferred to toluene by adding a toluene-dodecanethiol mixture (Au:S = 2:1), to obtain the colored organosol. A transmission electron microscope (TEM) image of the thiol-capped Au nanocrystals is shown in Fig. 1a. The complete transfer of the nanocrystals can be vividly seen from the color change of the two liquid phases (see inset in Fig. 1a). The particles are nearly spherical and highly monodisperse with a mean diameter of 4.1 nm as evident from the histogram of the size distribution in Fig. 1b. Furthermore, the nanocrystals form extended 2D arrays. The X-ray diffraction (XRD) pattern of the nanocrystal arrays exhibits a low-angle diffraction peak corresponding to a *d*-spacing of ~5 nm due to the formation of the assembly (Fig. 1c). The size of the nanocrystals could be varied by adjusting the concentrations of the Au ions and of the reducing agent. Assemblies of Pt and Ag nanocrystals could be similarly obtained by this method. This procedure is advantageous over other methods because the preparation of the

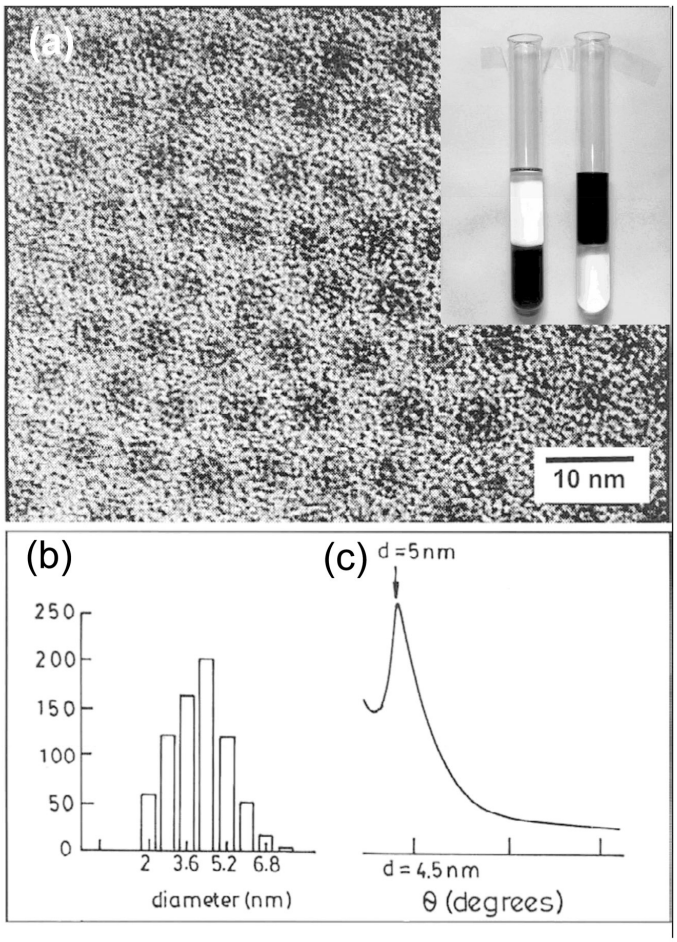

Fig. 1 (a) TEM image of a 2D array of Au nanocrystals of size ~4.2 nm. Inset shows the hydrosol (dark bottom layer) and the organosol (dark top layer) in toluene–water solvent pair. (b) Histogram showing the size distribution and (c) XRD pattern revealing a peak corresponding to the inter-particle spacing observed in the TEM image. (Reproduced from ref. [8].)

nanocrystals and their surface derivatization are in separate steps, thereby reducing surface contamination and providing a control over the size of the nanocrystals.

The process described above was extended to thiolize Pd nanocrystals [12] that were initially prepared in a hydrosol form by the method described by Teranishi and Miyake [13]. Pd nanocrystals with mean diameters ranging from 1.8 to 4.5 nm were prepared by the reduction of H_2PdCl_4 in water–ethanol mixtures in the presence of a suitable amount of polyvinylpyrrolidone. The hydrosol so obtained upon stirring with a thiol–toluene mixture in the presence of HCl resulted in the complete transfer of the nanocrystals from the aqueous layer to the organic layer.

Metal nanocrystals coated with thiols, silanes, phospholipids, or phosphines have been shown to organize spontaneously into superstructures on flat substrates [3]. Such assemblies give rise to novel properties and are key to the integration of nanocrystals into futuristic electronic devices. Seeking to understand the nature of such assemblies and the influence of the capping agents, some of us have carried out detailed investigations of the superlattice assemblies of Pd nanocrystals coated with alkanethiols of different chain lengths obtained by the procedure described earlier [12]. A TEM image of the hexagonally packed Pd nanocrystals coated with octanethiol is shown in Fig. 2a. The nature and the extent

of such assemblies were found to depend upon the chain length (l) of the ligating thiols as well as on the particle diameter (d). The butanethiol-coated Pd nanocrystals with a mean diameter of 4.5 nm form agglomerates. On the other hand, long-chain thiols such as octanethiol or dodecanethiol give rise to close-packed arrays that extend over several micrometers of area. The distance between two particles in an array depends on the extent of interdigation of the thiol molecules, which is determined by the diameter of the nanocrystals. These findings are supported by empirical calculations based on soft-sphere model and revealed that the ligated nanocrystals whose d/l values are in the range 1.5–3.8, form extended 2D hexagonal arrays with stabilization energies comparable to the thermal energy. Large nanocrystals ($d/l > 3$) with high stabilization energies form agglomerated structures while those attached to longer-chain thiols ($d/l < 1.5$) are associated with little stabilization and exhibit low-order structures. Based on the studies of nanocrystals with different d and l values, a phase diagram has been formulated (Fig. 2b). The bright area in the middle encompasses systems that form close-packed organizations.

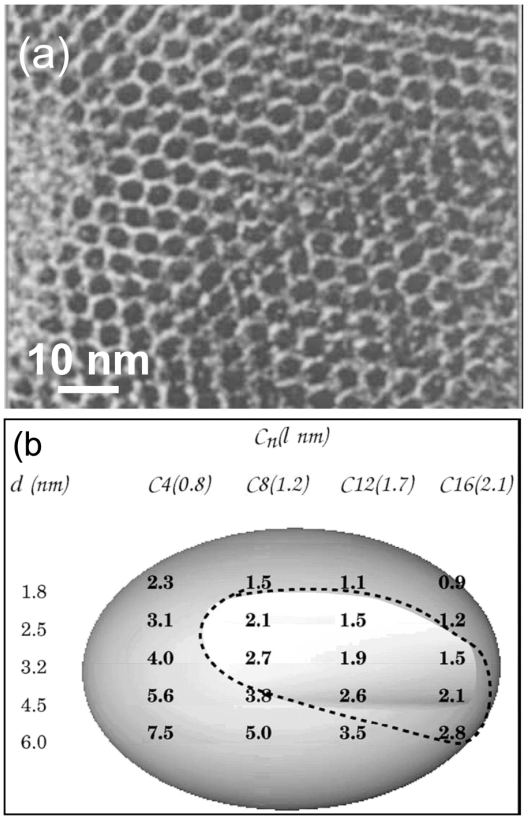

Fig. 2 (a) TEM image showing a hexagonal array of octanethiol-capped 3.2 nm Pd nanocrystals. (b) The d-l phase diagram for Pd nanocrystals capped with different alkane thiols. The surrounding darker area includes disordered or low-order arrangements of nanocrystals. The area enclosed by the dashed line is derived from calculations from a soft-sphere model.

Solvothermal synthesis of nanocrystals of metal oxides, chalcogenides, and nitrides

Metal oxide nanocrystals

Synthesis of pure CoO, which is an antiferromagnetic insulator (T_N = 298 K), is difficult due to its propensity to get readily oxidized [14,15]. It has been possible to carry out the decomposition of cobalt

cupferronate, [$Co(cup)_2$], under solvothermal conditions to obtain size-tunable CoO nanoparticles [16]. The solvothermal conditions afford high autogenous pressures inside the sealed autoclave that enable low boiling solvents to be heated to temperatures well above their boiling points. Thus, reactions can be carried out at elevated temperatures and the products obtained are generally crystalline compared to those from other solution-based reactions. Furthermore, the sealed reaction conditions reduce the possibility of atmospheric oxidation of the nanocrystals. In a typical reaction, 0.3 mmol of $Co(cup)_2$ was taken in 48 ml of decalin solvent, sealed in a Teflon-lined stainless steel autoclave, and heated at 270 °C for 48 h. The brownish-black precipitate obtained from the reaction was washed with toluene and ethanol. The size of the nanocrystals so obtained depends on the starting concentration of the reactants. TEM images of the 4.5- and 8.5-nm CoO nanocrystals shown in Figs. 3a and 3b suggest that the particles obtained in these syntheses are spherical with a narrow size distribution. A powder XRD pattern of the larger nanocrystals is shown in Fig. 3c. The nanocrystals exhibit interesting size-dependent magnetic behavior. For example, the antiferromagnetic transition found in bulk samples at ~300 °C is suppressed when the particle size becomes less than ~12 nm. In Fig. 3d, we show the temperature dependence of the dc magnetic susceptibility (χ) and inverse magnetic susceptibility (χ^{-1}) of the 11.5- and 16-nm nanocrystals. The smaller particles exhibit superparamagnetic behavior with magnetic hysteresis at low temperatures.

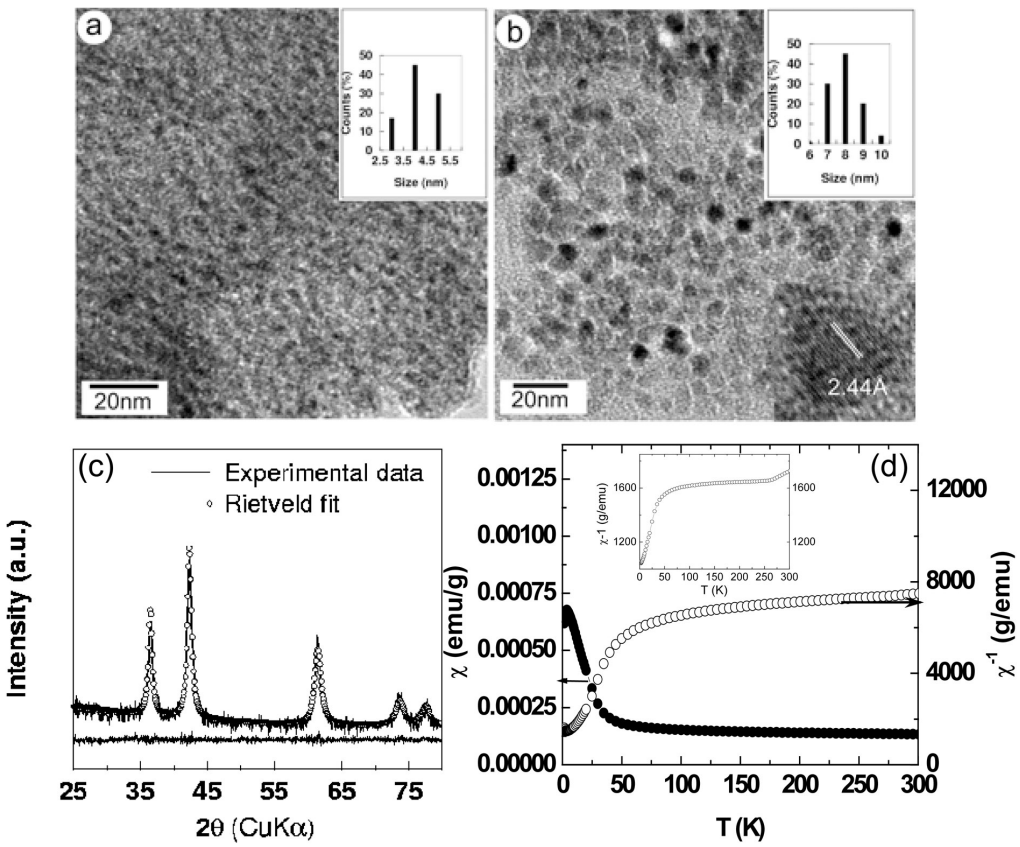

Fig. 3 TEM images of the CoO nanoparticles of (a) 4.5- and (b) 8.5-nm mean diameters. The insets show the histograms of the particle size distribution. The lower panel in (b) shows an HREM image of a single CoO nanoparticle. (c) XRD pattern of the 16-nm CoO nanocrystals. (d) Temperature dependence of dc magnetic susceptibility (χ) and inverse magnetic susceptibility (χ^{-1}) of 11.5-nm CoO nanocrystals. Inset in (d) shows the inverse susceptibility vs. temperature curve of 16-nm CoO.

ReO_3, in the history of transition-metal oxides, has a special place, being a metal with the luster and conductivity similar to that of copper [17]. Nanocrystals of ReO_3 have been prepared by the decomposition of the Re_2O_7-dioxane complex under solvothermal conditions [18]. The Re_2O_7-dioxane complex is obtained by dissolving Re_2O_7 in anhydrous 1,4-dioxane under mild heating and then reprecipitating the complex in an ice bath. To obtain ReO_3 nanocrystals, 2 ml of the ethanol solution of the complex was mixed with 45 ml of toluene, sealed in an autoclave, and inserted into a hot air oven at 200 °C. The autoclave was taken out after 4 h and allowed to cool to room temperature. The ReO_3 nanocrystals form a red dispersion in toluene and precipitate upon addition of ethanol. The size of the nanocrystals could be varied by adjusting the reaction conditions and the concentration of the starting dioxane precursor. Thus, the higher the reaction temperature, the longer the heating time, or the higher

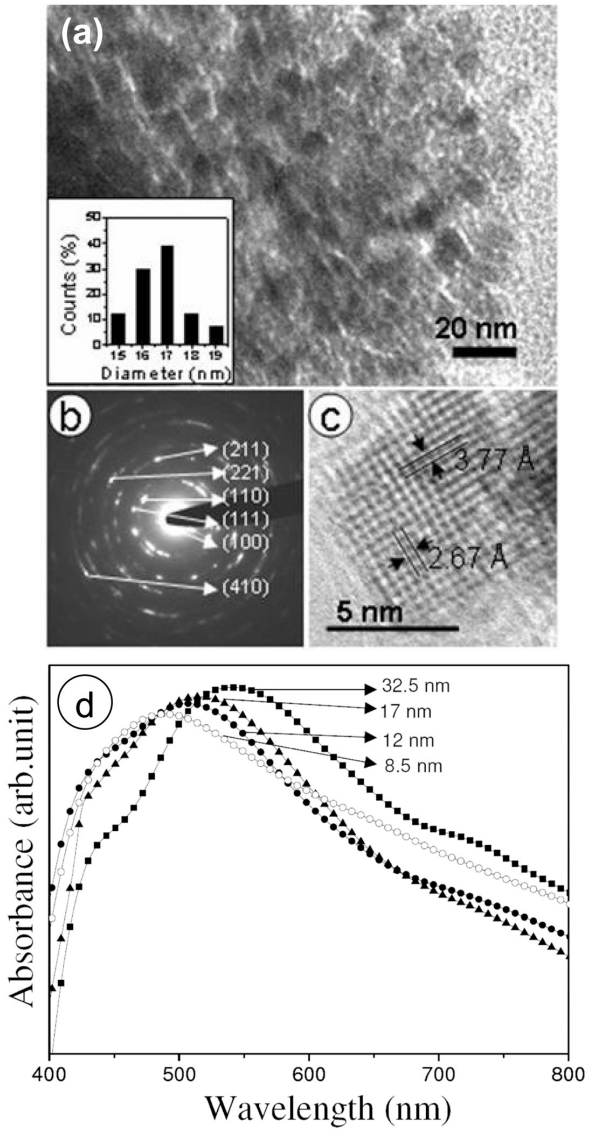

Fig. 4 (a) TEM image of 17-nm ReO_3 nanocrystals with the size distribution histogram in the inset. (b) Electron diffraction pattern of 17-nm nanoparticles. (c) HREM image of a particle. (d) Optical absorption spectra of ReO_3 nanocrystals with average diameters of 8.5, 12, 17, and 32.5 nm.

the precursor concentration, the larger the particle size. Nanocrystals with a mean diameter of 8.5 nm were obtained by using an ethanol solution of the dioxane precursor prepared from 0.048 mmol Re_2O_7. 17-nm nanocrystals were obtained under identical conditions but for the precursor solution that was prepared using 0.24 mmol Re_2O_7. A TEM image and the electron diffraction pattern of the 17-nm nanocrystals are shown in Figs. 4a and 4b, respectively. These nanocrystals are single-crystalline in nature as evident from the high-resolution electron microscope (HREM) image shown in Fig. 4c. The powder XRD pattern of the nanocrystals could be indexed on the *Pmim* (221) space group. The UV/vis absorption spectra of the nanocrystals of different diameters are displayed in Fig. 4d. The spectra clearly show that the λ_{max} of the plasmon absorption band [19] shifts to lower wavelengths with the decrease in particle size. Thus, the λ_{max} values are 543, 516, 507, and 488 nm, respectively, for the 32.5-, 17-, 12-, and 8.5-nm nanocrystals. Such blue-shifts in the λ_{max} with decreasing particle size are well known in the case of metal nanocrystals [20]. Magnetic measurements reveal that the 32.5-nm particles are diamagnetic at room temperature while 8.5-nm particles are paramagnetic. Magnetic hysteresis is observed at low temperatures in the case of the 8.5-nm particles, suggesting superparamagnetic behavior of the small particles. Magnetism in bulk ReO_3 is not yet fully understood, and there are conflicting reports of paramagnetic as well as diamagnetic behavior observed in this phase [21,22].

Metal chalcogenide nanocrystals

The solvothermal technique is ideally suited to prepare size-tunable, organic-soluble CdS nanocrystals [23]. Reactions of cadmium stearate [$Cd(st)_2$] with sulfur and tetralin in toluene solvent yield CdS nanocrystals. In this reaction, tetralin forms naphthalene, giving out hydrogen sulfide which reacts with $Cd(st)_2$ to yield the nanocrystals. Using capping agents such as trioctylphosphineoxide (TOPO) or dodecanethiol, the growth of the CdS could be arrested, giving rise to toluene-soluble monodisperse CdS nanocrystals. Thus, 4-nm dodecanethiol-capped CdS nanocrystals were obtained by the reaction of 0.68 mmol of $Cd(st)_2$, mixed with 0.68 mmol of sulfur, 0.75 mmol of tetralin, and 3.3 mmol dodecanethiol in 45 ml of toluene in a 70-ml Teflon-lined stainless steel autoclave at 220 °C. TOPO-capped CdS nanocrystals are prepared in a similar fashion. The TEM image of the TOPO-capped CdS nanocrystals in Fig. 5a shows that the particles are fairly monodisperse with a standard deviation of 0.4 nm (10 % of the mean). An HREM image of a single nanocrystal is shown as inset in Fig. 5a. The lattice fringes observed in the HREM images indicate a high degree of crystallinity. Using dodecanethiol, the reaction yielded CdS nanocrystals with mean diameters of 5 and 10 nm. The 5-nm nanocrystals are toluene-soluble, and the 10-nm ones are insoluble, thus making their separation feasible. Figure 5b shows the 5-nm thiol-capped CdS nanocrystals. The selected area electron diffraction (SAED) pattern of the nanocrystals is shown as the inset. The calculated *d* values from the SAED pattern match with those expected for the space group F-43m. It is interesting that the nanocrystals crystallize in the cubic structure rather than in the stable hexagonal structure. The powder XRD patterns of the 4-, 5-, and 10-nm CdS nanocrystals are displayed in Fig. 5c. The simulated XRD pattern of cubic CdS as shown in Fig. 5c (broken curve) matches well with the observed patterns. The UV/vis absorption spectrum of the nanocrystals shows a blue-shift of the absorption edge, indicating quantum confinement (Fig. 5d). Thus, the TOPO-capped 4-nm nanocrystals exhibit a well-defined absorption feature at 455 nm, considerably blue-shifted relative to the bulk value of 515 nm [24]. The method employed for CdS can be extended to prepare other metal chalcogenide nanocrystals as well. Toluene-soluble 3-nm CdSe nanocrystals have been prepared by reacting $Cd(st)_2$ with Se instead of sulfur [25]. The UV/vis absorption spectrum of the 3-nm nanocrystals shows an absorption band at 514 nm (bulk, 680 nm), consistent with quantum confinement. PbS and PbSe crystallites and nanorods can also be prepared by this method [26].

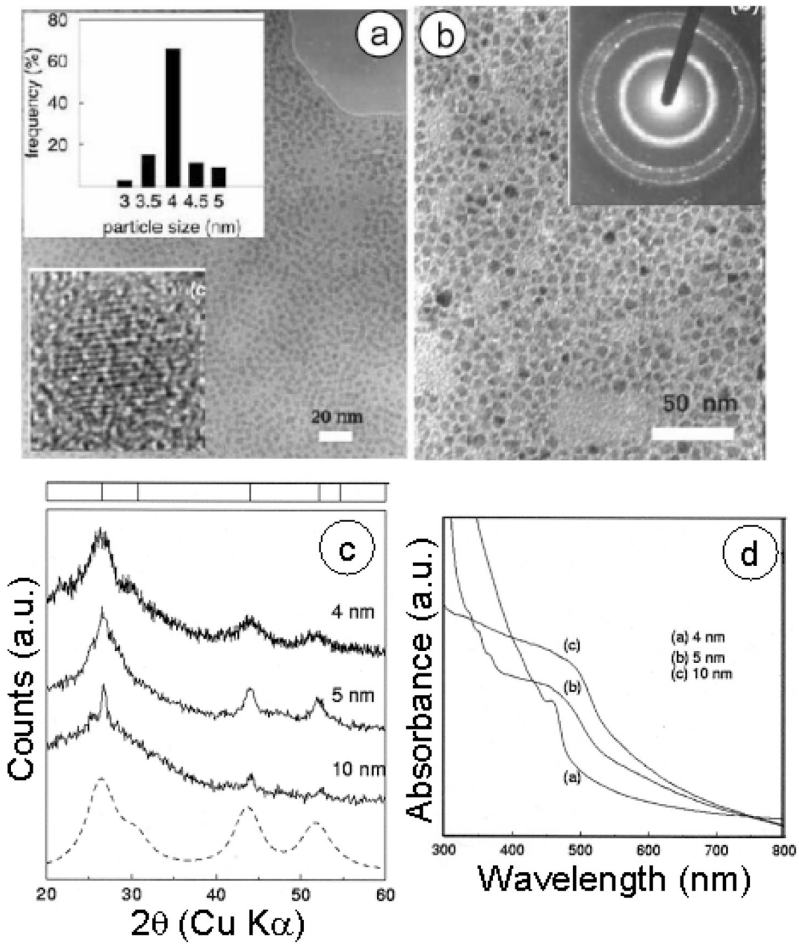

Fig. 5 TEM images of (a) TOPO-capped CdS nanocrystals (insets show the size distribution of the particles and an HREM image of a nanocrystal), (b) soluble dodecanethiol-capped CdS nanocrystals. Inset shows the electron diffraction pattern. (c) Powder XRD patterns of (i) 4-nm TOPO-capped, (ii) 5-nm soluble, and (iii) 10 nm-insoluble dodecanethiol-capped CdS nanocrystals. (iv) Simulated XRD pattern for the 4-nm particles. Vertical lines at the top represent expected peak positions. (d) UV/vis absorption spectra of the (i) 4-nm, (ii) 5-nm, and (iii) 10-nm CdS nanocrystals.

GaN nanocrystals

GaN and the related group III-V nitrides have drawn much attention due to the direct intrinsic bandgaps, which have allowed the fabrication of efficient light-emitting devices [27]. It is found that 1,1,1,3,3,3-hexamethyldisilazane ($Me_3SiNHSiMe_3$, HMDS) can be used as the nitriding agent for the synthesis of nanostructures of group III-V nitrides at relatively low temperatures [28,29]. A TEM image of the GaN nanocrystals obtained by the reaction of $GaCl_3$ with HMDS is shown in Fig. 6a. The reaction readily yields GaN nanocrystals by the elimination of volatile Me_3SiCl by-product. The inset in Fig. 6a shows the distribution of diameters of the GaN nanocrystals that lie between 5 and 15 nm. In Fig. 6b, we show the photoluminescence (PL) spectra of the GaN nanocrystals with mean diameters of 4 and 12 nm (prepared by the solvothermal reaction of gallium cupferronate, $Ga(cup)_3$ with HMDS) along with the PL spectrum of microcrystalline GaN particles prepared by NSP by the reaction of gallium acetylacetonate with NH_3 at 900 °C. While the 12-nm and 1-μm crystals show a broad band around 375 nm at excita-

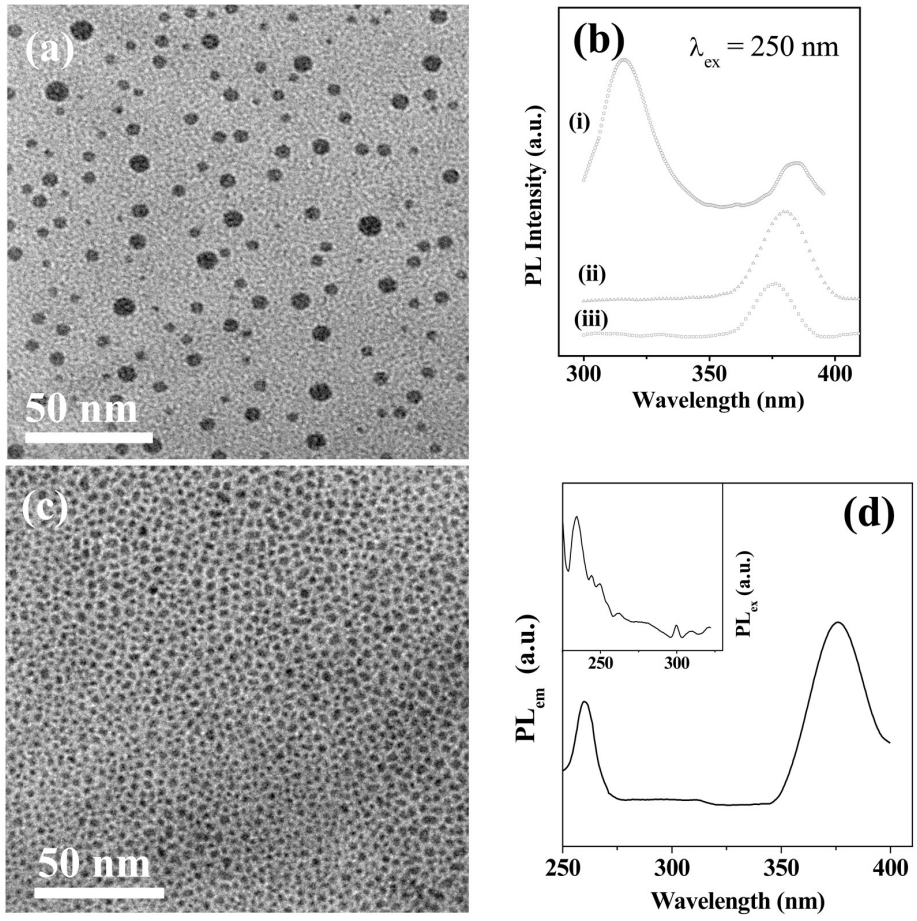

Fig. 6 (a) Typical low-magnification TEM image of the GaN nanocrystals obtained by the reaction of $GaCl_3$ and HMDS in presence of CTAB in toluene solvent under solvothermal conditions (inset shows histogram of particle size distribution). (b) Size-dependent PL emission spectra observed in GaN nanocrystals with varying diameters; (i) 4-nm, (ii) 12-nm, and (iii) micro-crystals. (Note the presence of an additional emission peak in the case of ~4 nm diameter nanocrystals, which is absent in other sets of particles with bigger average diameters). (c) TEM image of the ~2.5-nm GaN nanocrystals prepared by the reaction of $Ga(cup)_3$ with HMDS in the presence of CTAB as capping agent under solvothermal conditions (inset shows histogram of particle size distributions). (d) PL emission spectrum of the ~2.5-nm GaN nanocrystals (excitation wavelength 235 nm; inset shows PL excitation spectrum).

tion wavelengths of 250 and 260 nm, the 4-nm nanocrystals show an additional band around 315 nm, which we believe characterizes quantum confinement. The 375-nm band is insensitive to particle size as suspected [30,31]. The solvothermal reaction of $Ga(cup)_3$ with HMDS in the presence of *N*-cetyl-*N*,*N*,*N*-trimethylammonium bromide (CTAB) as the capping agent gave a narrow size distribution of the GaN nanocrystals. This has afforded nanocrystals of ~2.5 nm diameter as shown in the TEM image in Fig. 6c. The PL emission spectrum of these GaN nanocrystals exhibits bands 375 and 265 nm at an excitation wavelength of 235 nm (Fig. 6d). The 265-nm band is the blue-shifted band corresponding to the 315-nm band exhibited by the ~4 nm particles in Fig. 6b.

Nanocrystals generated at the liquid–liquid interface

A widely used technique for the preparation of assemblies or thin films of nanocrystals involves the air–water interface. The interface provides a constrained environment for the synthesis of nanocrystals in an organized manner which can be transferred as a film onto a substrate directly. There are several reports of nanocrystal assemblies of metals and semiconductors using the Langmuir–Blodgett (LB) method [32–34]. The interface between two immiscible liquids is a nonhomogenous region with a thickness of the order of few nanometers. This has a great deal of similarity with the air–water interface in terms of the surface tension, diffusion, and reaction kinetics. For example, the self-assembly of particles at liquid–liquid interfaces, driven by the reduction in interfacial energy as in the case of air–liquid interface, is well established [35]. There are, however, very few reports in the literature, on the use of the liquid–liquid interface to prepare nanocrystals and their aggregates. In one report, mixed cubic and hexagonal phases of CdS and CdSe thin films have been obtained by reacting an aqueous solution of Cd-carbonate with H_2S/H_2Se dissolved in CCl_4 in an LB trough [36]. The electrochemical deposition of Pt and Pd particles at the organic–water interface has been reported by Dryfe et al. [37].

The liquid–liquid interface has been exploited recently for obtaining ultra-thin nanocrystalline films of a variety of materials. The method involves dissolving an organic precursor of the relevant metal in the organic layer and the appropriate reagent in the aqueous layer. The product formed by the reaction at the interface contains ultra-thin nanocrystalline films of the relevant material formed by closely packed nanocrystals. This simple technique has been shown to yield nanocrystals of metals such as Au, Ag, and Pd, chalcogenides such as CdS and NiS as well as extended single-crystalline films of CuO, ZnO, CuS, CuS, PbS, and ZnS [32,38]. In a typical preparation of Au nanocrystalline films, 10 ml of a 1.5-mM solution of $Au(PPh_3)Cl$ in toluene was allowed to stand in contact with 16 ml of 6.25 mM aqueous alkali in a 100-ml beaker at 300 K. Once the two liquid layers were stable, 330 μl of 50-mM tetrakis-hydroxymethylphosphonium chloride (THPC) was injected into the aqueous layer using a syringe with minimal disturbance to the toluene layer [39]. The interface first appears pink, finally growing a robust Au film at the interface (Fig. 7a). This film could be converted either to a Au organosol or a hydrosol by using appropriate capping agents in the organic and aqueous layer, respectively, Figs. 7b and 7c. TEM investigations reveal that the film consists of reasonably monodisperse nanocrystals with mean diameters of ~7 nm as can be seen from the TEM image shown in Fig. 7d. HREM images show that the nanocrystals are single-crystalline, as shown in the inset at the center of Fig. 7. The image shows distinct (111) planes with a separation of ~2.3 Å.

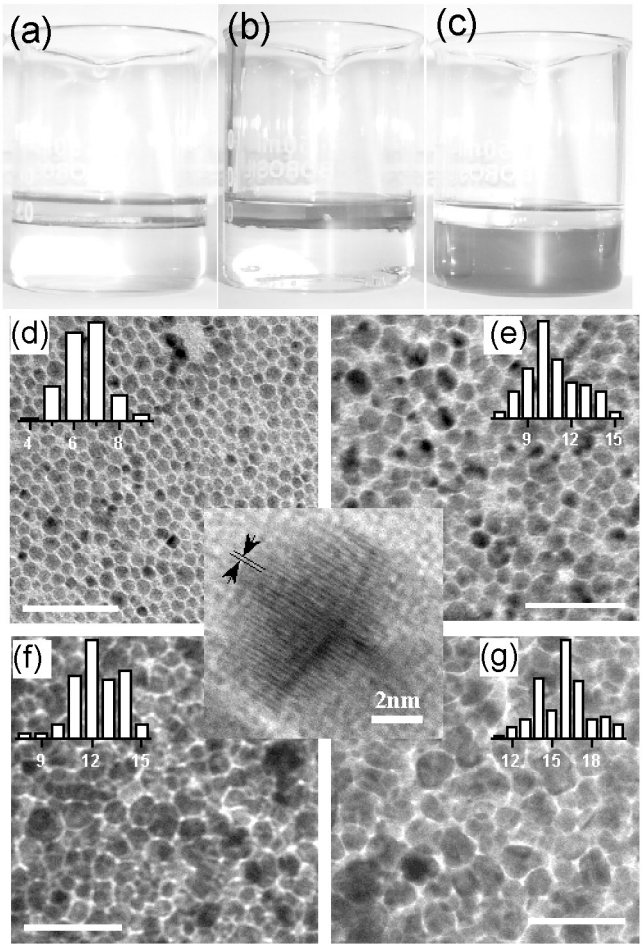

Fig. 7 (a) Nanocrystalline film of Au formed at the toluene–water interface, (b) when dodecanethiol is added to the toluene layer, the film breaks up, forming an organosol of Au, (c) Au hydrosol obtained when mercaptoundecanoic acid is added to water later. TEM images of the ultra-thin nanocrystalline Au films obtained at the liquid–liquid interface at after 24 h: (d) 30 °C, (e) 45 °C, (f) 60 °C, and (g) 75 °C. The histograms of particle size distribution are shown as insets. The scale bars correspond to 50 nm. An HREM image of an individual particle is shown at the center.

Scanning electron microscope (SEM) and atomic force microscope (AFM) studies of the films reveal fairly smooth and continuous nature of the film over several tens of microns, apart from a few micropits and cracks. AFM images also reveal that the thickness of the films at the interface is of the order of ~100 nm. The image in Fig. 8a shows a boundary of the Au film on a mica substrate. The height profile in Fig. 8b gives an estimate of the thickness to be ~60 nm. The thickness and the particle size of the nanocrystals were found to be dependent on the reaction conditions employed, such as reactant concentrations, reaction time, and temperature. For example, the TEM images of the nanocrystalline Au films obtained at different temperatures are shown in Fig. 7. The mean diameters of the nanocrystals formed at 30, 45, 60, and 75 °C are 7, 10, 12, and 15 nm respectively. Interestingly, the electron transport measurements on the films show a metal to insulator transition, the films formed at room temperature (30 °C) having high resistance in the MΩ range, while that of the 45 °C film is in the kΩ range. The resistance of the films formed at higher temperatures is of the order of few ohms, showing metal-

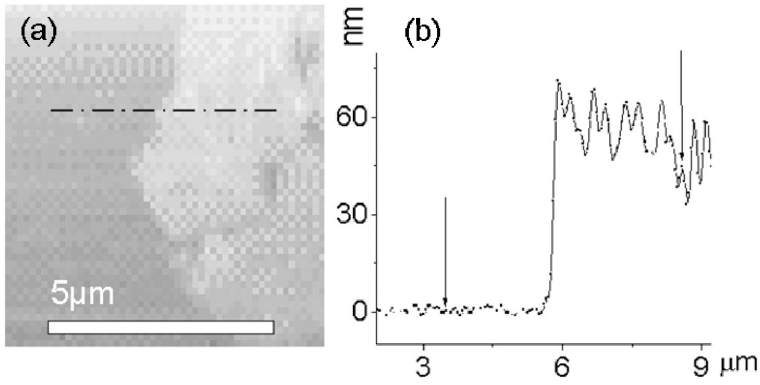

Fig. 8 (a) Contact-mode AFM image showing the boundary of Au film on a mica substrate. (b) The *z*-profile along the line shown in (a).

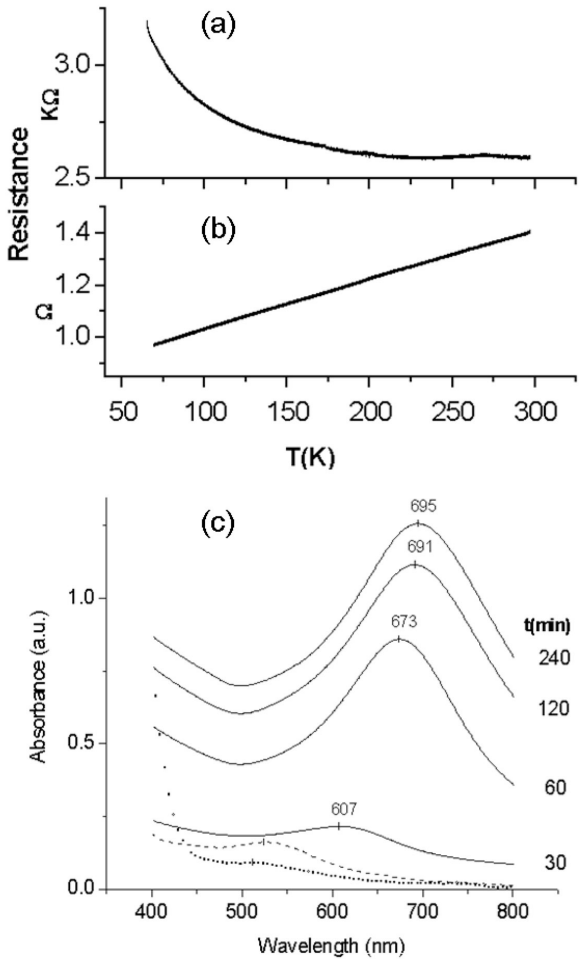

Fig. 9 Temperature variation of the electrical resistance of the Au films prepared at (a) 45 °C and (b) 75 °C (current used, 10 mA). (c) Evolution of the electronic absorption spectra with the growth of the nanocrystalline Au film at the interface at 45 °C (full curves). Spectra of octylamine-capped Au nanocrystals in toluene (broken line) and mercaptoundecanoic acid-capped nanocrystals in water (dotted line) are also shown.

lic behavior (see Figs. 9a and 9b). The plasmon peak of the Au nanocrystals (~600 nm) [20] increases in intensity accompanied by red-shifts in the initial stage of the reaction (Fig. 9c). The band does not show any variation after 120 min of the reaction due to the saturation of the growth process.

The liquid–liquid interface has been employed to prepare nanocrystalline films of binary alloys of Au–Ag and Au–Cu, and also ternary Au–Ag–Cu alloys [40], by starting with an appropriate mixture of the corresponding metal precursors. A TEM image of a nanocrystalline Au–Ag film is shown in Fig. 10a. The composition of the films could be confirmed using spot X-ray energy dispersion analysis (EDAX) measurements, which showed that the stoichiometry of the precursor mixture was retained in the films as well. In addition, the composition was found to be uniform over large areas of the film as shown in the elemental map in Fig. 10b. The Au–Ag alloy films could be disintegrated to form the organosols in toluene by addition of octadecanethiol. The organosol of Ag is known to exhibit the surface plasmon band at 420 nm [41]. The plasmon band of the alloy sols appears between those of monometallic sols, the position varying proportionally with the composition (Fig. 10c).

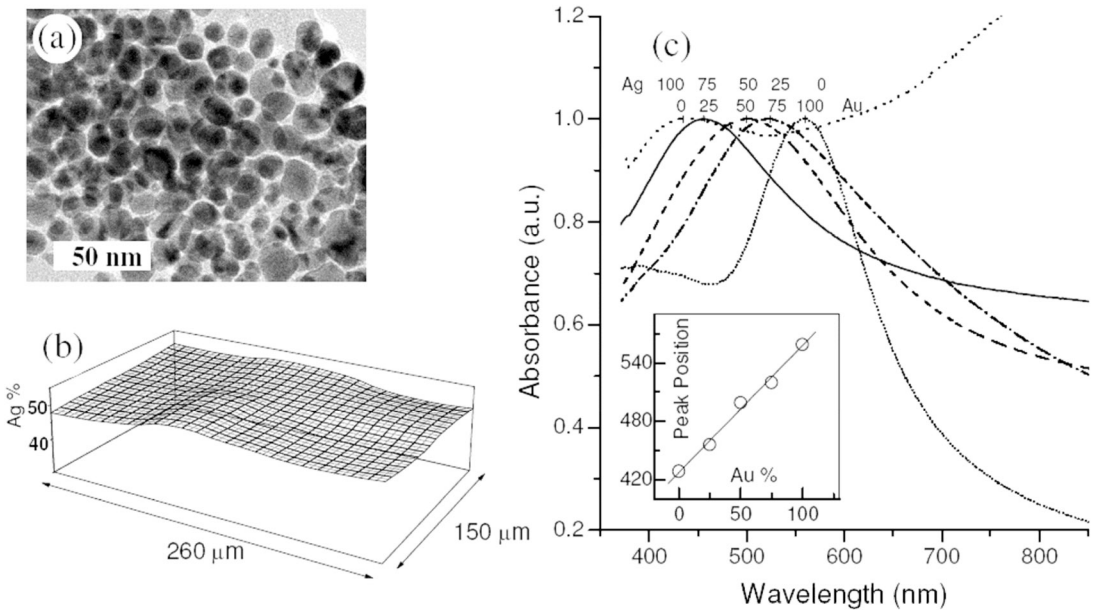

Fig. 10 (a) TEM image of the Au–Ag alloy nanocrystals (Au:Ag = 50:50). (b) Elemental map obtained from EDAX measurements at various locations of a film. (c) Optical absorption spectra of Au–Ag alloy sols with different compositions.

Nanocrystalline films of metal chalcogenides such as CdS, CoS, and NiS have been prepared at the toluene–water interface. In a typical preparation of a CdS film, 0.0045 g of Na_2S was dissolved in 30 ml of water (2 mM) in a 100-ml beaker and 0.0125 g of cadmium cupferronate [$Cd(cup)_2$], was dissolved in 30 ml of toluene (1 mM) by ultra-sonication [42]. A few drops of *n*-octylamine were added to the $Cd(cup)_2$ solution in order to make it completely soluble. The toluene solution was slowly added to a beaker containing the aqueous Na_2S solution. The interface started appearing yellow within a few minutes, and a distinct film was formed after 10 h. The film could be lifted onto various substrates with the help of forceps. We obtained 5.5-nm nanocrystals of CdS upon sonication of this film (Fig. 11a). The powder XRD pattern of the film showed that the CdS nanocrystals crystallize in the rock-salt structure rather than in the usual wurtzite structure. The size of the nanocrystals formed at the interface depends on the reaction conditions as well as the choice of solvent. 6.5-nm CdS nanocrystals were obtained by carrying out this reaction at 75 °C. Increasing the concentration of the reactants yielded bigger

nanocrystals. The size of the nanocrystals could be reduced by controlling the diffusion rate of the S^{2-} ions. Thus, nanocrystals of 3.5-nm diameter were obtained by doubling the viscosity of the aqueous medium by using a 24 mass % glycerol–water mixture. The UV/vis spectrum of the 5.5-nm CdS nanocrystals (Fig. 11b) shows a broad absorption maximum around ~450 nm, which is blue-shifted compared to the bulk CdS (absorption maximum at 515 nm) due to quantum confinement. The 3.5-nm nanocrystals show the band at ~340 nm. The PL spectrum of the 5.5-nm particles shows a peak at 610 nm. In a similar fashion, nanocrystals of other metal sulfides such as CoS and NiS could also be prepared.

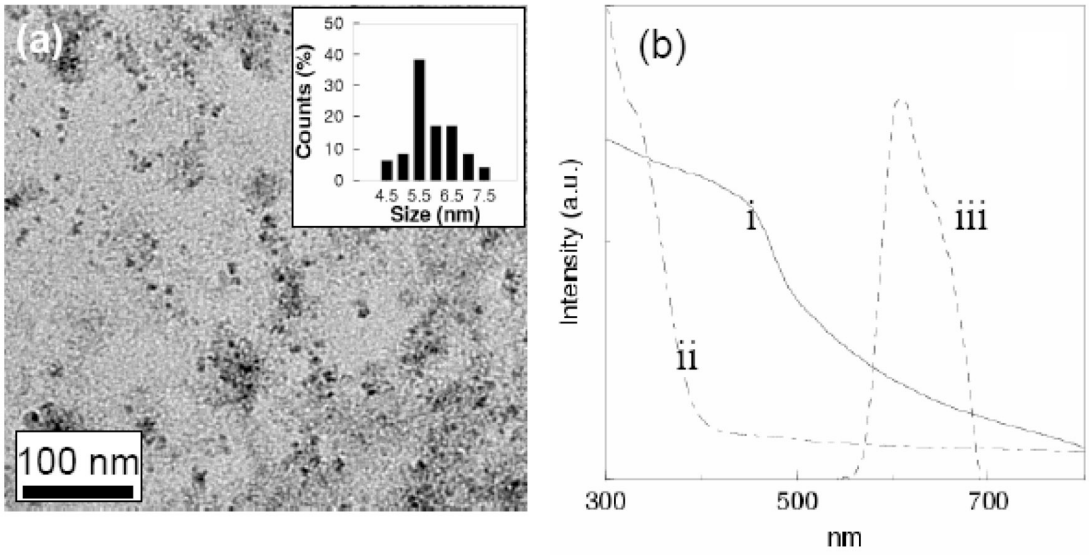

Fig. 11 (a) TEM image of 5.5-nm CdS nanocrystals obtained at room temperature at the interface (inset gives the particle size distribution). (b) UV/vis absorption spectra of (i) 5.5-nm, (ii) 3.5-nm CdS nanocrystals. (iii) PL emission spectrum of 5.5-nm CdS nanocrystals.

NANOWIRES AND NANOTUBES

Se and Te nanowires

Se, with a direct bandgap of 1.3 eV [43], exhibits a number of interesting properties such as a high photoconductivity (~8×10^4 Scm^{-1}), and finds commercial applications in photography and xerography [44]. Te has a narrow direct bandgap of 0.35 eV [43] and is known for its catalytic activity as well as piezoelectric, thermoelectric, and nonlinear optical responses [45]. These two elements have identical crystal structures. As can be seen from Fig. 12a, trigonal Se (*t*-Se) consists of helical chains of covalently bonded Se atoms, bound together through van der Waals interactions. Se and Te would be expected to have a tendency to form 1D structures favoring the stronger covalent bonds along the *c*-axis over the weak forces between the chains. We have synthesized nanorods of *t*-Se employing a simple solution-based method [46]. In this method, Se powder is first reacted with $NaBH_4$ in water to yield NaHSe [47], which being unstable decomposes to give amorphous Se. In a typical room-temperature reaction, 0.025 g (0.32 mmol) of Se was mixed with 20 ml of deionized water in a three-necked round bottom flask. 0.030 g (0.81 mmol) of $NaBH_4$ was added to this mixture, and the flask was purged with nitrogen gas in order to create an inert atmosphere. Se dissolves in water in 60 min, giving rise to a clear colorless solution. The reactions involved are:

$$4NaBH_4 + 2Se + 7H_2O \rightarrow 2NaHSe + Na_2B_4O_7 + 14H_2 \quad (1)$$

$$Na_2B_4O_7 + 2NaHSe + 2Se + 5H_2O \rightarrow 2Na_2Se_2 + H_3BO_3 \quad (2)$$

$$Na_2Se_2 + 2H_2O \rightarrow 2Se\ (\text{amorphous}) + 2NaOH + H_2 \quad (3)$$

$$Se\ (\text{amorphous}) \rightarrow t\text{-}Se \quad (4)$$

The nascent Se produced in step (3) imparts a wine red color to the aqueous solution. On standing for a few hours, the solution transforms into amorphous Se in colloidal form. A small portion of the dissolved Se precipitates as *t*-Se nanoparticles, which act as nuclei to form 1D nanorods. The XRD pattern of the product in Fig. 12b shows changes in the relative intensities of the diffraction peaks as compared to that of bulk indicating growth of 1D structures. An SEM image of the nanorods is shown in Fig. 12c. The diameter of the rods is around 150 nm, having lengths of several micrometers. The HREM image shown in Fig. 12d reveals that the rods are single-crystalline, devoid of crystallographic defects. The lattice spacing of 4.9 Å in the HREM image along the growth direction corresponds to the separation between the (001) planes, showing thereby that the growth direction is along the *c*-axis, as ex-

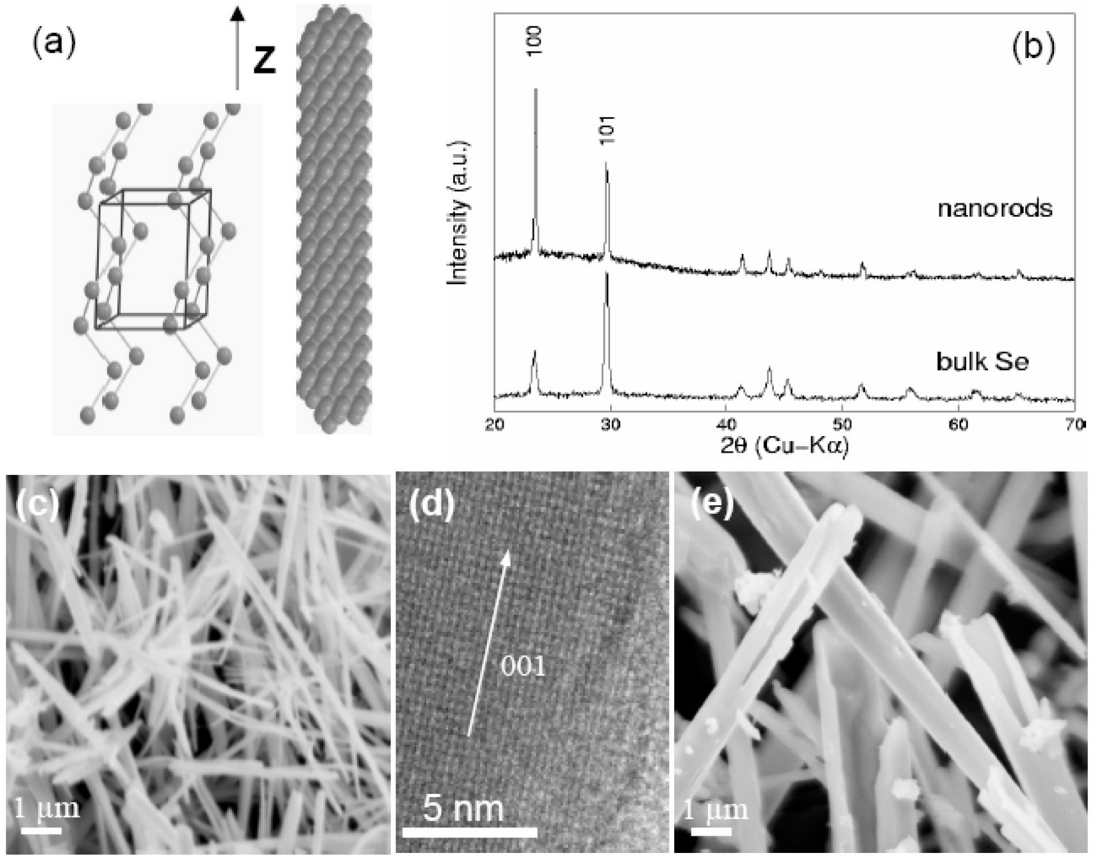

Fig. 12 (a) Crystal structure of *t*-Se showing a unit cell with helical chains of covalently bonded Se atoms extended along the *c*-axis. The growth direction of the 1D nanostructures is shown along with an atomic model of a rod. (b) XRD patterns of the *t*-Se nanorods and bulk Se powder used as the starting reagent. (c) SEM image of the Se nanorods obtained after 4 days by reacting 0.025 g of Se with 0.03 g of $NaBH_4$ in 20 ml water. (d) An HREM image of one of the nanorods (arrow indicates the growth direction of the nanorods). (e) SEM image of the scroll-type *t*-Se obtained under hydrothermal conditions.

pected. Shorter nanorods were obtained when the reaction mixture was quenched at 0 °C for 96 h. The diameter of the nanorods could be decreased by diluting the reaction mixture. Thus, 20-nm nanorods were obtained when the reaction mixture was diluted four times. The nanorods assemble in bundles. The reaction carried out under solvothermal conditions gives tubular structures, with a wall thickness of the order of 100 nm (Fig. 12e).

Extending the above strategy, Te nanorods, nanowires, nanobelts, and junction nanostructures have been obtained [48]. The reaction of Te (0.030 g) with $NaBH_4$ (0.050 g) in aqueous medium gave uniform nanowires of 100–300 nm diameter with lengths of approximately 10 μm (Fig. 13a). The nanorods grow with time and become smoother and monodisperse as time passes. Figure 13b shows an HREM image of one of the nanorods. The fringe spacing of 5.8 Å observed in the image corresponds to the separation between the (001) planes of hexagonal Te. The image reveals that the growth of the nanorods is perpendicular to this plane and hence along the (001) direction. The HREM image and the SAED pattern of the rods (see inset in Fig. 13b) confirm the single-crystalline nature of the rods. The dimensions of the Te nanorods depend on the initial concentrations of the reactants. When the reaction was carried out with 0.300 g of Te powder and 0.500 g of $NaBH_4$ in 20 ml of water, interesting morphologies were obtained. In Fig. 13c, we show an SEM image of the feather-like structures obtained in such a preparation. When a reaction mixture of 0.0300 g of Te powder and 0.0500 g of $NaBH_4$ was diluted with 150 ml of hot deionized water, just after the dissolution of the Te powder, uniform nanorods

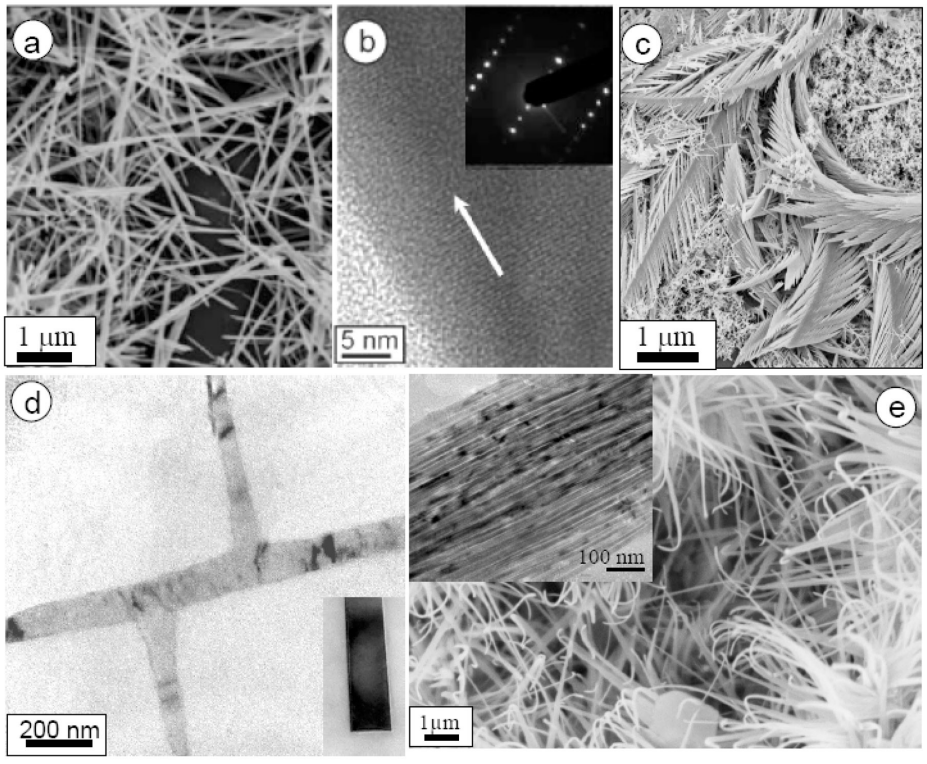

Fig. 13 SEM images of (a) nanorods obtained from the reaction of 0.03 g of Te with $NaBH_4$ in 20 ml of water, (b) HREM image of a Te nanorod showing the (001) lattice planes of *t*-Te. The growth direction is shown with an arrow. Inset shows the corresponding SAED pattern. (c) Feather-like structures obtained with high reactant concentrations (0.3 g of Te powder in 20 ml of water). (d) Nanobelts containing T-junctions and similar structures obtained by hydrothermal synthesis. Inset shows tip of a nanobelt. (e) SEM image of aligned nanorod bundles. The aligned bundles are seen in the TEM image shown as inset.

of 20 nm diameter and 400 nm length were obtained. Unlike solution-phase synthesis, where uniform nanorods were obtained, the same synthetic procedure under hydrothermal conditions at 150 °C yielded crystalline Te nanobelts. The thickness of the belts was 5–10 nm. An interesting feature of the nanobelts is their tendency to form branches and junctions as shown in Fig. 13d. When the reaction was carried out in the presence of sodium dodecylbenzenesulfonate, aligned nanobelts were obtained (Fig. 13e). TEM investigations revealed that each of the 1D nanostructures seen in the SEM image is actually a bundle of much smaller aligned nanobelts (shown as inset in Fig. 13e).

Single-source precursor route to 1D nanostructures

$Fe_{1-x}S$ and $GeSe_2$ nanowires

Magnetic nanowires are considered important due to their potential applications in magnetic storage devices. There are some reports describing the preparation of nanowires of magnetic materials such as Fe, Co, Ni, and their alloys [49–51]. Among the magnetic metal sulfides, $Fe_{1-x}S$ has a complex phase dia-

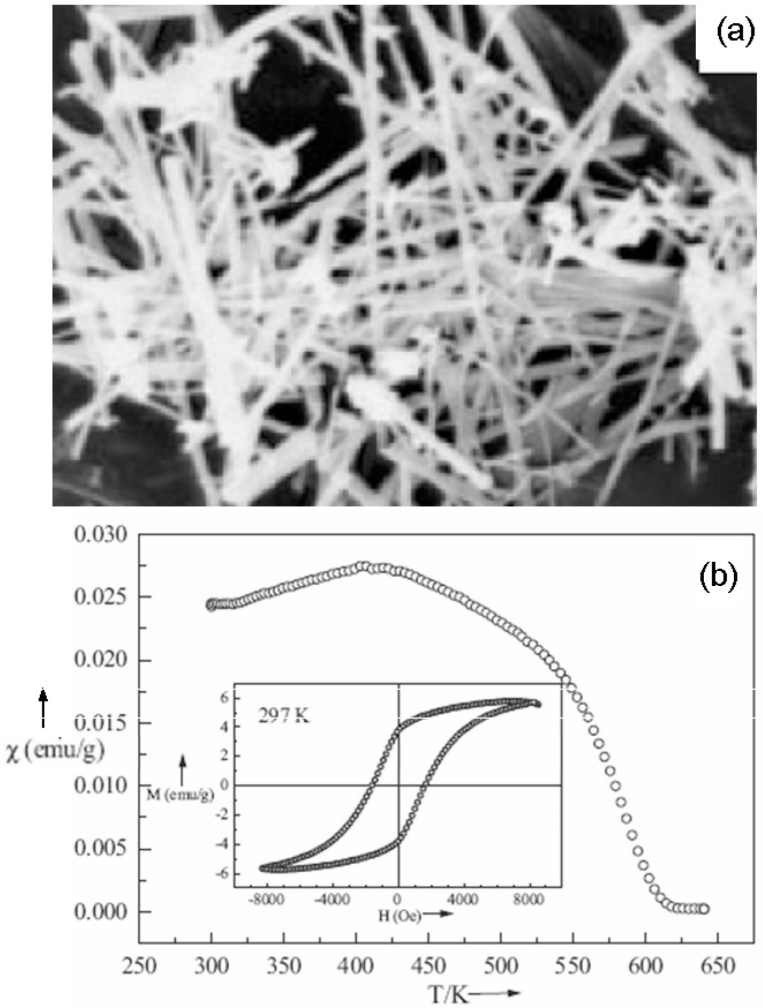

Fig. 14 (a) SEM image of $Fe_{1-x}S$ nanowires. (b) The temperature variation of magnetic susceptibility. Inset shows the hysteresis loop obtained at 297 K.

gram with a broad range of compositions between FeS and FeS_2 [52]. These phases possess distinct magnetic and electronic properties which depend on the exact composition of the phase. In order to investigate the properties on a nanoscale, a new strategy was developed to synthesize iron sulfide nanowires that involves the thermal decomposition of organic–inorganic composite, $Fe_{1-x}S(en)_{0.5}$ (en: ethylenediamine) [53]. This precursor composite can be prepared by solvothermally heating a mixture of ferrous chloride and thioacetamide (taken in the ratio 1:2) at 180 °C in ethylenediamine solvent. The product exclusively contains $Fe_{1-x}S(en)_{0.5}$ nanowires having diameters of 80–150 nm and lengths of several micrometers. Elemental analysis showed Fe-to-S ratio to be in the range of 0.7–0.8 in these compounds. Finally, to prepare Fe_7S_8 nanowires, the precursor composite was taken in a quartz boat, placed in a horizontal furnace and heated at 200 °C for 30 min under Ar gas flow. An SEM image of the Fe_7S_8 nanowires is given in Fig. 14a. The nanowires retain the morphology of the precursor composite, suggesting a templated growth mechanism for the 1D nanostructures. Magnetic measurements show a ferrimagnetic behavior with a transition temperature of 600 K (Fig. 14b), characteristic of Fe-$_7S_8$. The nanowires also show a hysteresis loop at room temperature (297 K). The saturation magnetization was 6 emu/g with an applied field of 1000 Oe. The remnant magnetization and coercivity was found to be 4 emu/g and 2000 Oe, respectively.

Toward finding other single-molecular precursors for nanostructures, we have developed a new organoammonium germanium selenide, which upon heating, decomposes to yield $GeSe_2$ nanowires

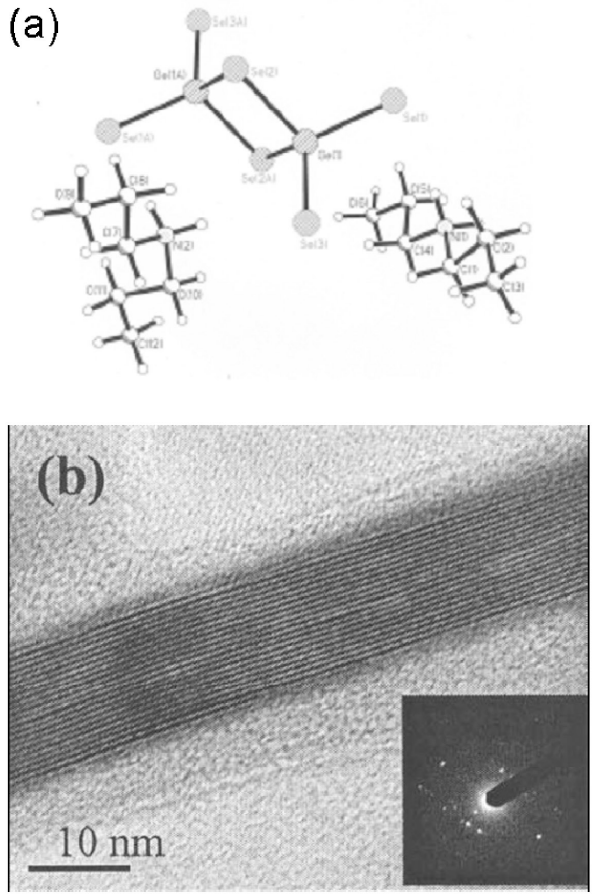

Fig. 15 (a) The structure of the molecular precursor $[C_6H_{14}NH_2]_4[Ge_2Se_6]$ showing the Ge_2Se_6 dimer and the amine. (b) HREM image of a $GeSe_2$ nanowire. The inset shows a typical SAED pattern.

[54]. The precursor, $[(C_3H_7)_2NH_2]_4[Ge_2Se_6]$ was prepared solvothermally from metallic Ge and Se powders heated in the presence of dipropylamine. Its crystal structure consists of isolated cations (dipropylammonium ions) and $[Ge_2Se_6]^{4-}$ anion, which is an edge-shared dimer of $GeSe_4$ tetrahedra (Fig. 15a). Such a structure can be expected to facilitate the formation of $GeSe_2$. In a typical preparation of $GeSe_2$ nanowires, $[(C_3H_7)_2NH_2]_4[Ge_2Se_6]$ was thermally decomposed in a horizontal tube-furnace at 450 °C under a flow of Ar (180 sccm) + H_2 (20 sccm). After the completion of the reaction, the furnace was cooled to room temperature and the blackish product containing $GeSe_2$ nanowires was collected from the sample boat (yield 50%). The mean diameter of the nanowires is ~30 nm, and their lengths measure up to a few micrometers. An HREM image of a $GeSe_2$ nanowire is shown in Fig. 15b. The image as well as the SAED pattern (inset in Fig. 15b) indicate the single-crystalline nature of the nanowires. The lattice fringes of 5.8 Å in the HREM image corresponds to the separation between the (002) planes of monoclinic $GeSe_2$.

III-V nitride nanowires

Synthesis of the III-V nitrides from single-molecular sources provides a simple solution to what is otherwise a complex problem. Considering that such a one-pot synthesis of the nitride nanostructures is desirable, we have explored the use of a simple and common single-source precursor route for group 13 metal nitride semiconductor nanostructures. Our synthetic approach of III-V nitride nanowires follows the Au-nanocluster catalyzed vapor–liquid–solid (VLS) growth process (Fig. 16) [4]. In this procedure, the urea complex of the metal nitrides, $Al(NH_2CONH_2)_6Cl_3$, $Ga(NH_2CONH_2)_6Cl_3$, and $In(NH_2CONH_2)_3Cl_3$ undergo thermal decomposition to form M–N–Au (where M = Al, Ga, and In) droplets, followed by nucleation and growth of nanowires when the droplets get saturated with reactants. In order to achieve high yields of nanowires on selected regions of Si(100) substrates, Au nanoclusters were coated (10–50 nm thick) in the form of islands by a DC sputtering technique using the help of a mask. In each reaction, approximately 30–100 mg of the single-source precursor was heated in an appropriate atmosphere inside a quartz tube furnace at a desired temperature. The AlN nanowires grow in the 900–1100 °C temperature range. However, better crystallinity was obtained from reactions carried out above 1000 °C. For the growth of GaN nanowires, the precursor was heated at 800–900 °C for 3–6 h. Straight and smooth hexagonal InN nanowires were prepared by the decomposition of $In(NH_2CONH_2)_3Cl_3$ in the presence of the Au islands in a very narrow temperature range (550–585 °C) for 6–12 h. Below this temperature range, a mixture of In_2O_3 and InN is formed, and above this temperature, InN decomposes to indium metal thereby causing In metal impurity in the sample. The aspect ratio of the nanowires could be controlled by varying the precursor concentration as well as the size of Au islands.

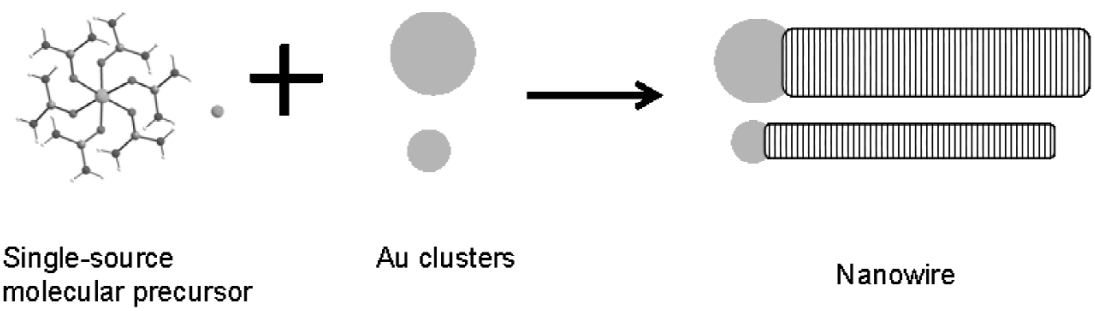

Fig. 16 Schematic of III–V nitride nanowire growth from single-source molecular precursor via a Au nanocluster-catalyzed VLS mechanism.

The grazing incidence (1°) XRD pattern of the AlN nanowires (Fig. 17a) confirms the hexagonal structure with lattice parameters $a = b = 3.095$ Å, $c = 5.040$ Å. Unlike earlier reports [55], a cubic phase was not detected in the AlN sample. An SEM image of the AlN nanowires is given in Fig. 17b showing high yields. The nanowires are not straight and smooth, instead entangled with each other as observed from the SEM and low-magnification TEM images. The grazing incidence (1°) XRD pattern (Fig. 17c) of the GaN nanowires on Si(100) substrates revealed hexagonal structure with lattice parameters, $a = b = 3.196$ Å, $c = 5.219$ Å. The yield of the nanowires is high, as can be inferred in the SEM image in Fig. 17d. The nanowires are smooth and straight with diameters in the 50–100-nm range and lengths of 1–2 μm as observed in the low-magnification TEM image. The presence of Au clusters at the tip of the nanowires (in the TEM images) confirms the proposed VLS mechanism (Fig. 16) for the growth of the nanowires. Figure 17e shows the grazing incidence (1°) XRD pattern of InN nanowires obtained by thermal decomposition of $In(H_2NCONH_2)_3Cl_3$ in a NH_3 atmosphere at 550 °C on a selective area Au-coated Si(100) substrate. The nanowires have hexagonal structure with lattice

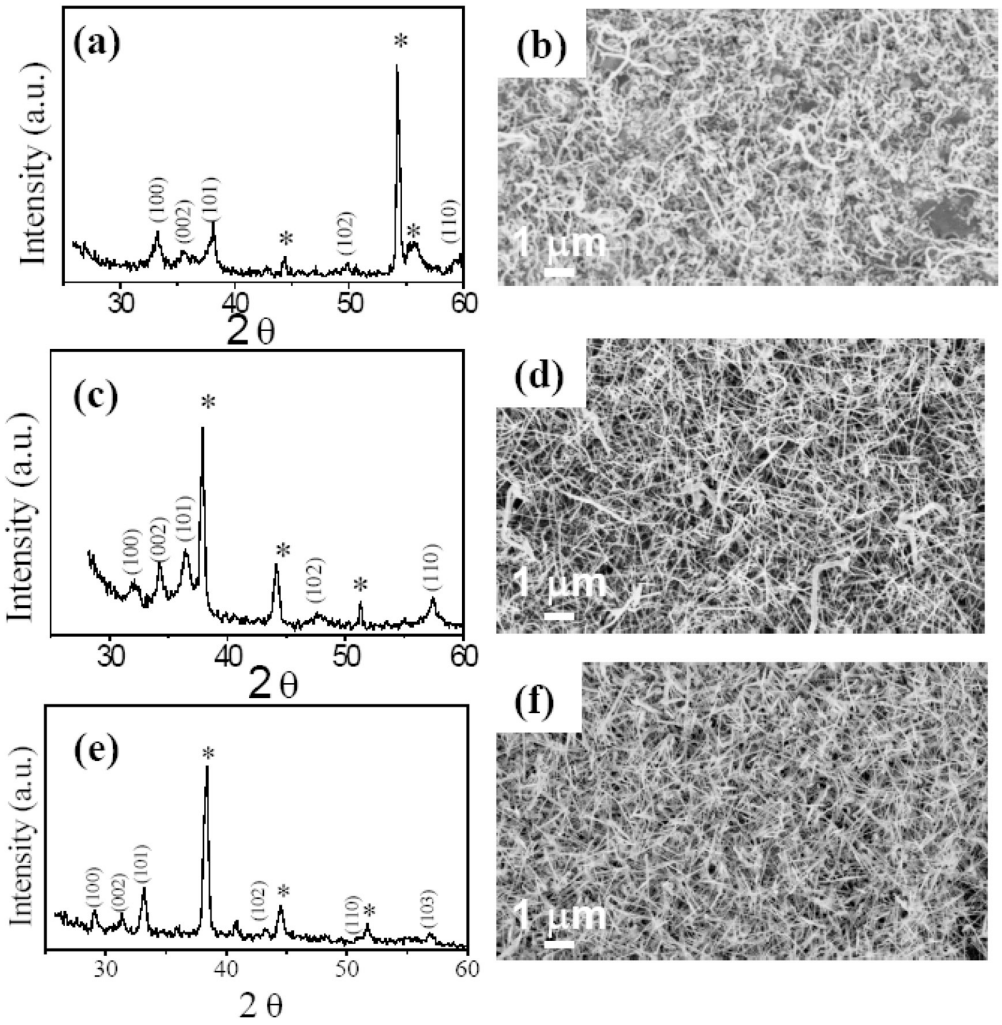

Fig. 17 XRD patterns and SEM images of (a), (b) AlN; (c), (d) GaN and (e), (f) InN nanowires, respectively, prepared using single-source molecular precursors (asterisks indicate peaks arising due to Si substrates or Au catalyst particles).

parameters, $a = b = 3.527$ Å, $c = 5.733$ Å. A typical SEM image of the InN nanowires obtained by this procedure is displayed in Fig. 17f. The nanowires have diameters in the range of 20–100 nm with lengths up to 1–3 μm.

Surfactant-assisted synthesis of CdS and CdSe nanotubes and nanowires

The synthesis of 1D nanostructures of II-VI semiconductor chalcogenides has been much less explored in comparison to elemental and metal oxide nanowires. It has been possible to synthesize nanowires and nanotubes of these materials by a relatively simple chemical method wherein surfactants such as t-octyl-$(OCH_2CH_2)_9OH$, (Triton-X) and sodium bis(2-ethylhexyl) sulfosuccinate (AOT) are used as templates [56,57]. A typical procedure to prepare cadmium sulfide nanostructures was as follows. A suspension of the cadmium oxide (10 mmol) and AOT was prepared in 30 ml cyclohexane. 40 ml aqueous solution of 10 mmol thioacetamide in an acidic or basic medium (HCl or NaOH was used to liberate S^{2-}) was added drop-wise to the emulsion, under stirring. The reactant mixture was then refluxed in an inert atmosphere at ~40–60 °C for 16 h. The product obtained was washed thoroughly with ether and dried. Triton-X was used as the surfactant directly (without any cyclohexane), and the refluxing temperature was ~105 °C. In order to prepare cadmium selenide nanostructures, a solution of NaHSe ($NaBH_4$/Se in 50 ml water) was used instead of thioacetamide solution, and the reaction was carried out under inert conditions. The reaction product contained high yields of either nanowires or nanotubes depending upon the concentration of the surfactant used. A Triton X-100 concentration of 16 mmol generally yielded nanowires, whereas a higher surfactant concentration of 24–40 mmol predominantly yielded nanotubes (Fig. 18a). The nanowires are generally polycrystalline with diameter and length in the ranges of 40–160 nm and 3–4 μm, respectively. In the case of nanotubes, outer diameter is in the 15–20-nm range, while the diameter of the central tubule is in the 10–15-nm range (Fig. 18b). XRD analyses establish the hexagonal crystal structures of the chalcogenides. The procedure was easily extended to prepare polycrystalline nanowires of CuS, ZnS, CuSe, and ZnSe having diameters in the range of 5–150 nm and high aspect ratios.

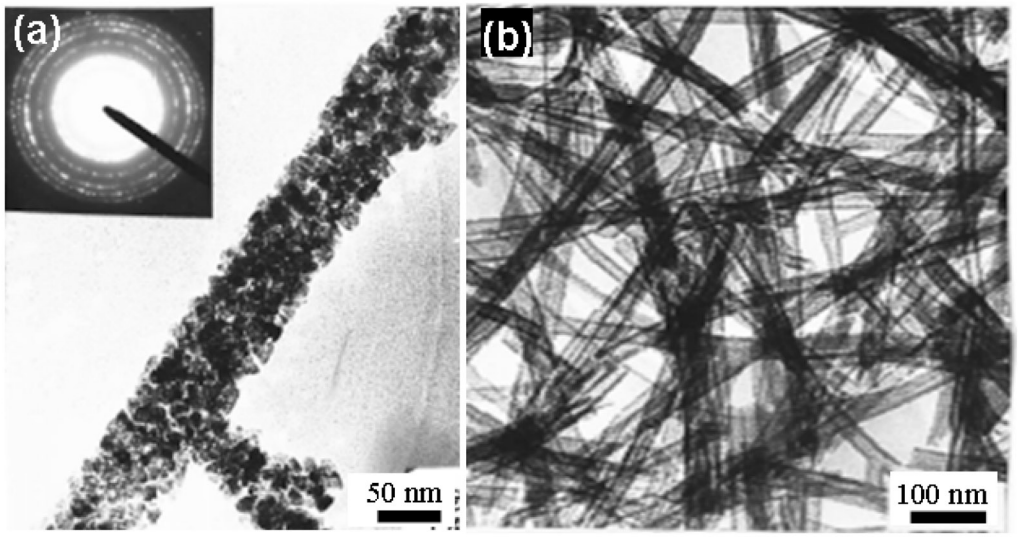

Fig. 18 TEM images of (a) CdS nanowires, (b) CdSe nanotubes obtained by using Triton X-100 as the surfactant. Inset in (a) shows the electron diffraction pattern of the CdS nanowires.

Hydrogel route to nanotubes of metal oxides and sulfates

Low-molecular-weight organogelators gel solvents at low concentrations due to the formation of a 3D network owing to their fibrous aggregation in organic fluids. The self-assembled organogelators have been employed as templates to obtain nanotubes of several materials such as silica [58] where metal alkoxides are used as precursors. However, due to difficulties in synthesizing as well as handling metal alkoxides, the use of hydrogels has been explored. Thus, nanotubes of oxides such as SiO_2, TiO_2, ZrO_2, WO_3, and ZnO, and of sulfates such as water-soluble $ZnSO_4$ and of $BaSO_4$ have been obtained employing a tripodal cholamide-based hydrogel method [59]. The spontaneous aggregation of tripodal cholamides, having hydrophobic surfaces, into gel fibers in predominantly aqueous media is known in the literature [60]. In a typical reaction for the synthesis of silica nanotubes, 0.03 mmol of the tripodal cholamide was dissolved in 0.4 ml CH_3COOH and to this, 1.6 ml H_2O and 0.1 ml of tetraethyl orthosilicate (TEOS) were added. The contents were thoroughly mixed and left undisturbed at room temperature. Gel fibers soon formed, simultaneously accompanied by the hydrolysis of TEOS around them. After 24 h, the gel was dried in vacuum to obtain gel fibers coated with silica. The outer diameters of the tubes are in the range of 30–40 nm and inner diameter of ~5 nm. The nanotubes have lengths extending to a few hundred nanometers. In a similar fashion, titania nanotubes with similar inner diameters and outer diameters of 10–20 nm were obtained using tetrabutyl orthotitanate. XRD analysis of the TiO_2 nanotubes showed them to be in the anatase phase. ZnO nanotubes were obtained using a Zn acetate and KOH mixed solution.

Readily water-soluble nanotubes of $ZnSO_4$ were prepared by starting from an ammonical solution of 0.19 mmol $ZnSO_4$ in 1.6 ml H_2O with a drop of NH_3 to which a solution containing 20 mg gelator in 0.4 ml CH_3COOH was added. A white gel so obtained was dried in vacuum. The nanotubes have an inner diameter of ~4 nm and an outer diameter in the 10–12-nm range with lengths of 200–300 nm. The advantage of this method is that nanotubes of a desired diameter can easily be made by a suitable choice of the hydrogelator or by slightly modifying the gelation conditions. Besides, this opens up new avenues to synthesize nanotubes that were previously difficult to synthesize using traditional methods.

Synthesis of 1D nanostructures by NSP

1D nanostructures of various materials including multi-walled carbon nanotubes (MWNTs) have been prepared by NSP of precursor solutions. A detailed discussion of the NSP technique has been presented elsewhere [61–64]. Nebulized spray is a spray generated by an ultrasonic atomizer [65]. When a high frequency (100 kHz–10 MHz) ultrasonic beam is directed to a gas–liquid interface, a geyser forms at the surface. The formation of the geyser is accompanied by the generation of a spray, resulting from the vibrations at the liquid surface and cavitation at the gas–liquid interface. The properties of spray such as diameter of droplets, the amount of material transported depends on the solvent parameters such as surface tension, density, saturated vapor pressure, and ultrasonic excitation frequency.

Carbon nanotubes

Pyrolysis of a metallocene in a two-stage furnace is a simple and versatile route for the preparation of various types of carbon nanotubes [66]. The main variables in the experiment are sublimation rate of metallocene, the flow rate of the carrier gas, and the pyrolysis temperature. The disadvantage of this method is that the reaction stops after the complete sublimation of the metallocene and poor control over the sublimation rate of metallocene. To overcome these problems, nebulized spray was employed to pyrolize metallocene. The process is continuous and has a good degree of control over the metallocene supply rate for pyrolysis. For the growth of MWNTs, metallocene is dissolved in a hydrocarbon solvent such as toluene and the solution is nebulized using a 1.54 MHz ultrasonic beam carried into a 25-mm quartz tube placed inside a SiC furnace maintained between 800–1000 °C. Argon was used as a carrier gas, and its flow rate was controlled using mass flow controllers. It is possible to control the

diameter distribution and the quality of the nanotubes by varying parameters such as catalyst precursor concentration, type of solvent, pyrolysis temperature, and carrier gas flow rate.

Figure 19 shows representative electron micrographs of MWNTs obtained by this method under different conditions. The method in general yields MWNTs (Fig. 19a), and large arrays of aligned MWNT bundles are obtained when mesitylene is used a solvent for ferrocene as seen Fig. 19b. MWNTs with a narrow size distribution are obtained by the NSP of 20 g/l ferrocene in toluene was carried out along with acetylene (Fig. 19c). An HREM image of a MWNT obtained by the NSP of $Fe(CO)_5$ and acetylene is shown in Fig. 19d.

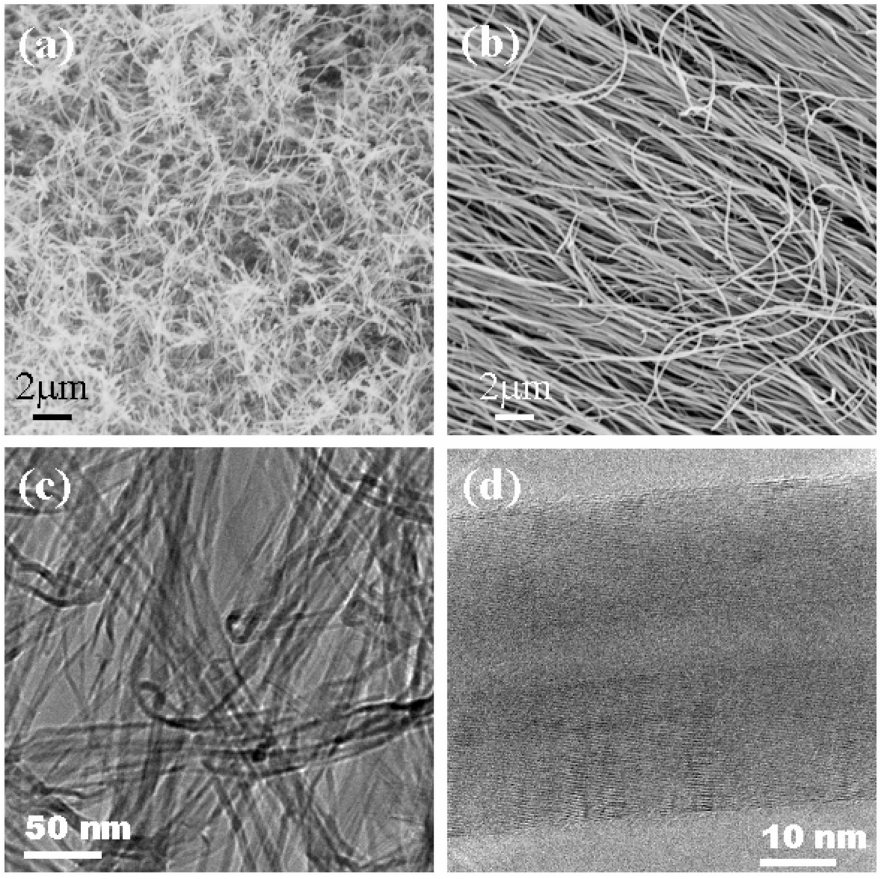

Fig. 19 (a) and (b) SEM images of the product obtained by the NSP of 20 g/l ferrocene in toluene and mesitylene, respectively. (c) TEM image of aligned MWNT bundles obtained by NSP of 20 g/l solution of ferrocene for 5 min and acetylene flow rate of 100 sccm for 30 min, (d) HREM image of MWNT obtained by pyrolysis of $Fe(CO)_5$ in the presence of 100 sccm acetylene. All the experiments carried out at 900 °C with argon (Ar) carrier gas.

Metal nanowires

NSP of a methanolic solution of metal acetates yields metal nanowires [67]. The versatility of the method is demonstrated by the synthesis of single-crystalline nanowires of Zn, Cd, and Pb. The nanowires were synthesized using the same experimental set-up described elsewhere [4,67], and they are deposited at the outlet of the quartz tube. The nanowires obtained are in high yields as seen in the SEM images in Figs. 20a and 20b. The nanowires have no catalyst particles at their ends as seen in

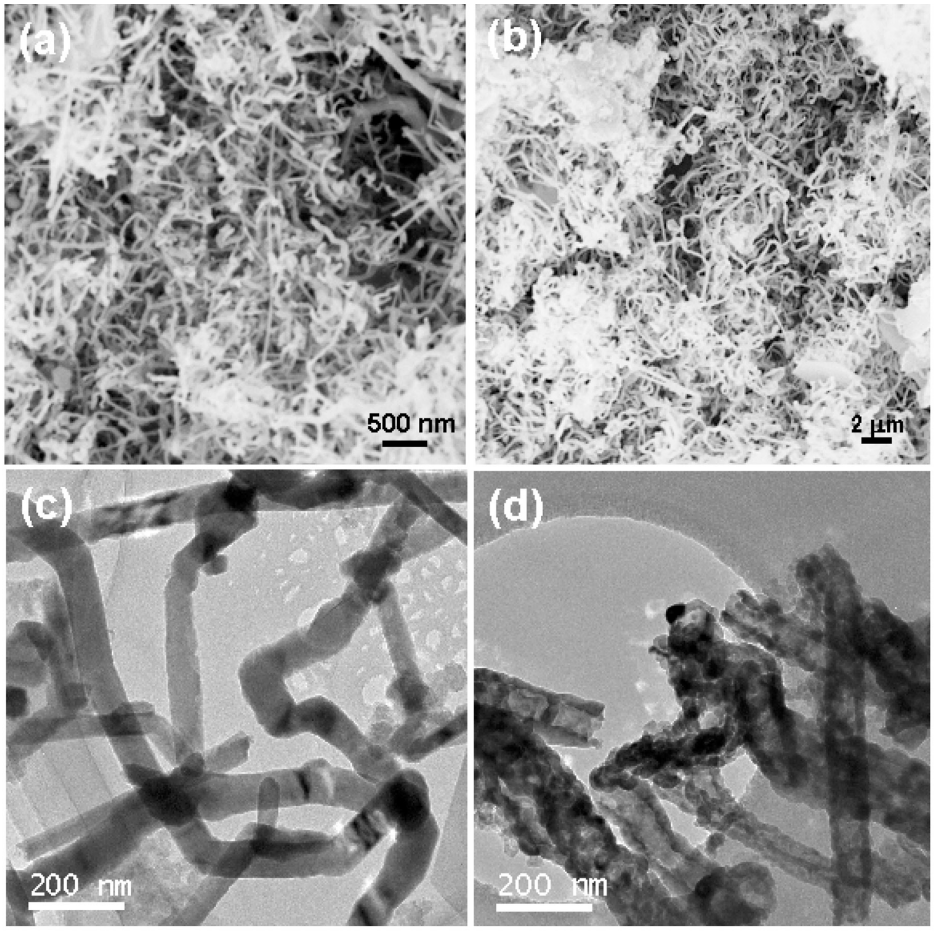

Fig. 20 (a), (b) SEM images of Zn and Cd nanowires obtained by the pyrolysis of the corresponding metal acetates at 900 °C. (c) TEM image of Zn nanowires (inset shows SAED pattern taken on a single nanowire) and (d) TEM image of ZnO nanotubes obtained by the oxidation of Zn nanowires at 450 °C.

Fig. 20c, thus suggesting a vapor–solid (VS) growth mechanism. Zn nanowires on oxidation at 450 °C yield ZnO nanotubes as seen in the TEM image in Fig. 20d.

Semiconductor nanowires

1D nanostructures of GaN and InN with a direct bandgap of ~3.4 and 1.9 eV at room temperature are ideal candidates for future generation of nanodevices for optoelectronic applications [68,69]. The primary concerns in the growth of these materials are reduction of structural defects, control over diameter, high morphological yield, and cost. Several growth methods have been developed and employed in the literature [70–72]. The NSP technique can also be used to grow single-crystalline pure hexagonal GaN and InN nanowires with high aspect ratios and very high morphological yield by the reaction of metal acetylacetonate, ($M(acac)_3$, where M = Ga and In) with NH_3 employing a Au-catalyzed VLS mechanism [73].

Typical SEM images of the GaN and InN nanowires prepared by NSP and deposited on Au islands covering Si(100) substrates are shown in Figs. 21a and 21b, respectively. The GaN nanowires have the wurtzite structure with $a = b = 3.198$ Å, $c = 5.210$ Å was obtained by the NSP technique. Low-magnification TEM images along with the SAED pattern of individual GaN nanowires are shown in

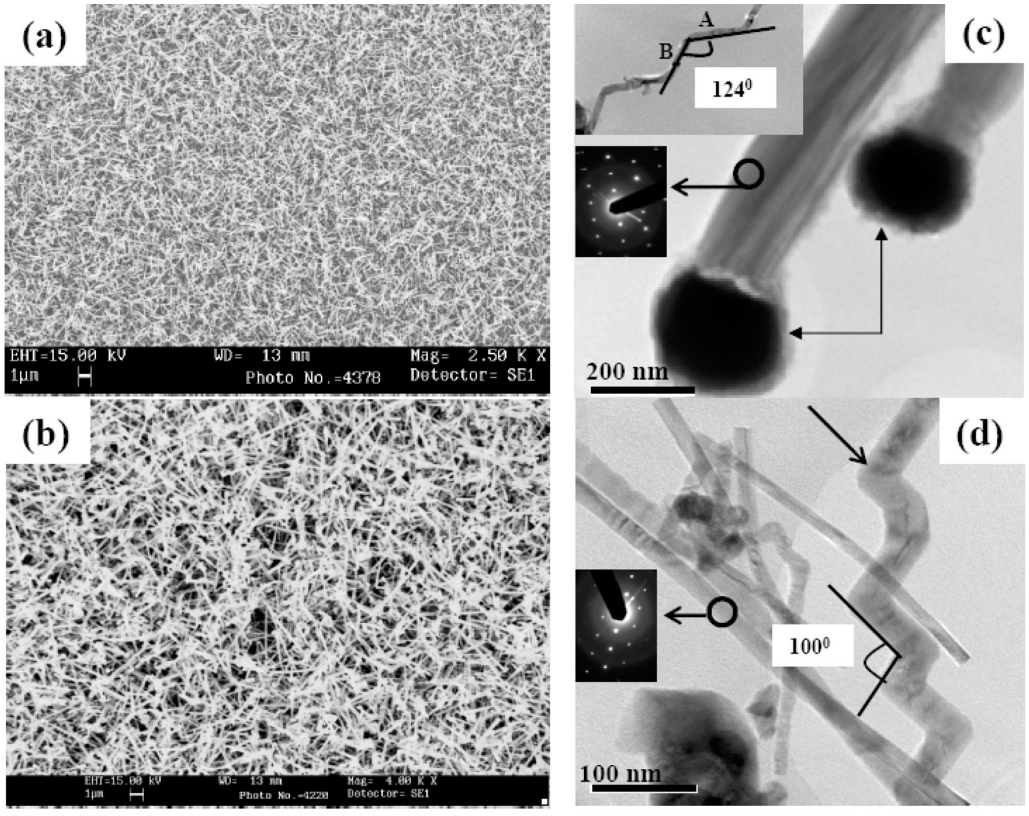

Fig. 21 (a), (b) SEM images of GaN and InN nanowires, respectively, prepared by NSP. (c), (d) Low-magnification TEM images of GaN and InN nanowires, respectively (presence of Au catalyst particles at the tip of the nanowires is shown by arrows in (c)). Inset in (c) shows an unusual zigzag-type GaN nanowire. Inset in (d) shows SAED pattern of an InN nanowire. Presence of zigzag-type InN nanowire is shown by an arrow in (d).

Fig. 21c. The average diameters of the nanowires are in the 10–80-nm range and lengths around 1000 nm. The black spherical particles at the tip of the nanowires are the Au catalysts. The presence of such catalyst particles at the tips confirms the VLS growth mechanism. The nanowires are single-crystalline in nature as revealed by the spots in the SAED patterns on different nanowires (see inset in Fig. 21c). We have also observed zigzag-shaped GaN 1D nanostructure with two segments (A and B in the inset of Fig. 21c). The zigzag-type structure is similar to that found earlier on Si and GaN nanowires [74,75]. The zigzag-shaped nanostructures are likely to be formed by the self-stacking of (0001) planes of the wurtzite structure.

The InN nanowires grown by NSP have the hexagonal structure with $a = b = 3.540$ Å, $c = 5.790$ Å. Low-magnification TEM image (Fig. 21d) shows nanowires with diameters in the range of 10–40 nm. We have also observed periodic zigzag-type InN nanowire with an angle of 100° (shown by an arrow in Fig. 21d) between two alternate segments. The nanowires are single-crystalline as found from the SAED pattern (see inset of Fig. 21d).

GaS and GaSe nanotubes

The discovery of inorganic fullerenes and nanotubes by Tenne and coworkers [76] created a great deal of interest in the synthesis of similar types of nanostructures made up of other layered materials such

as WS_2, MoS_2, NbS_2, BN, BC_3, $NiCl_2$, and CN, etc. [4,76–79]. Thin layers of these materials are energetically unstable and tend to roll up in order to eliminate the dangling bonds at the periphery of the layers; leading to the formation of fullerenes and nanotubes. III-VI semiconductors, GaS, and GaSe possess identical layered structures, which consist of double layers of the metal atoms sandwiched between double layers of the non-metal atoms. In GaS, the layers contain four sheets of Ga and S atoms stacked along the *c*-axis in the sequence S–Ga–Ga–S, with two such layers in a unit cell. On the basis of theoretical calculations, Cote et al. [80] predicted that GaSe with a layered structure should form nanotubes similar to carbon nanotubes. They found that the strain energy of GaSe nanotubes was comparable to that of carbon nanotubes and should have inner diameters of ~5 nm. Kohler et al. [81] have proposed that GaS with a layered structure should also form nanotubes. However, there is no report on the formation of fullerene structures and nanotube structures by GaS and GaSe. It has been shown recently that nanotubes of GaS and GaSe can be obtained by solvent-assisted laser irradiation. Polycrystalline powders of GaS or GaSe were dispersed in a liquid medium such as *di*-tert-butyldisulfide, toluene, or *n*-octylamine and irradiated for 2 min by using a Q-switched Nd:YAG laser [82]. Laser irradiation of GaS powder leads to the exfoliation, creating thin layers of GaS which roll over to form tubular or fullerene structures. Figure 22a shows a TEM image revealing the rolling of an exfoliated GaS sheet. TEM investigations revealed presence of nanotubes in laser irradiation product, (Fig. 22b). Figure 22c

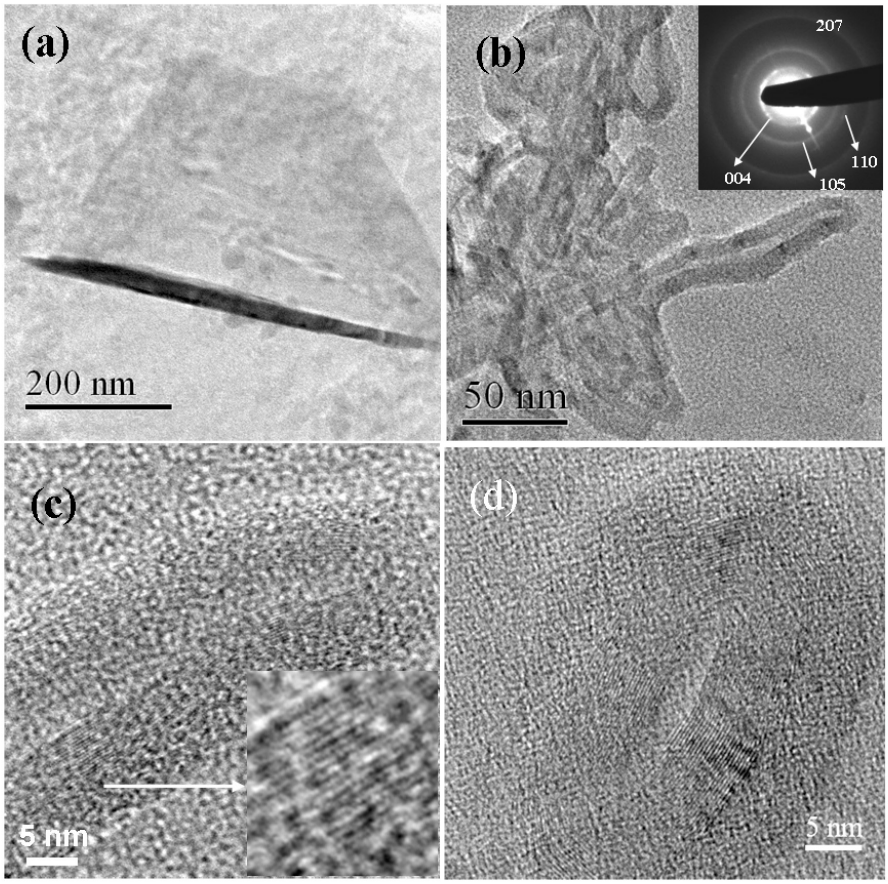

Fig. 22 TEM image revealing (a) rolling of an exfoliated GaS layer, (b) GaS nanotubes obtained by solvent-mediated laser irradiation. (c) HREM image of a nanotube (d = 3.15 Å). (d) TEM image of a GaSe onion obtained by laser irradiation in *n*-octylamine.

shows an HREM image of a wall of a nanotube, showing an interlayer spacing of 3.15 Å corresponding to the separation between (100) planes of GaS. There is a small lattice expansion of 1.5 % commonly seen in such nanostructures [79]. Laser irradiation of GaSe powder in *n*-octylamine also gave nanotubes and onion-like structures. A GaSe onion is shown in Fig. 22d. Direct laser irradiation of solid GaS yields amorphous particles, and a suitable solvent medium is essential in order to obtain nanotubes.

A good yield of highly crystalline GaSe nanotubes was obtained by thermal exfoliation technique in which its powder was heated in a sealed quartz tube to 900 °C [76]. One end of the tube was kept at ~400 °C in a vertical furnace. Heat treatment of GaSe powder gave rise to flower-like deposits that also contained nanotubes and onions. A TEM image of the nanotubes is shown in Fig. 23a. The nanotubes have closed spherical or conical tips. The HREM images of the nanotubes in Fig. 23b and 23c give a lattice spacing of ~3.46 Å corresponding to the spacing between the (100) planes of hexagonal GaSe.

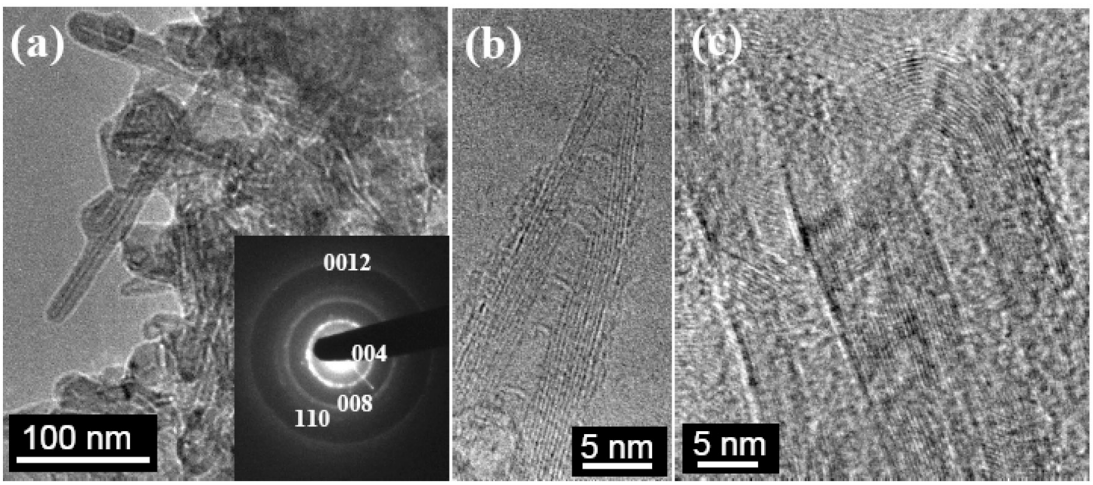

Fig. 23 (a) TEM image of the GaSe nanotubes obtained by thermal exfoliation. (b), (c) HREM images of the nanotubes.

TWO-DIMENSIONAL NANOSTRUCTURES

Nanowalls

Thermal exfoliation of GaS and GaSe gives rise to nanowalls. Nanowalls of carbon, which are actually interconnected 2D nanosheets of carbon vertically standing on a substrate, have been described by Wu and coworkers [7]. There are reports of ZnO nanowalls and ZnO nanorods grown from the nodes of nanowalls [83]. As mentioned in the previous section, thermal exfoliation of GaSe gave rise to solid deposits in the cooler end of the sealed tube [84]. Deposits with similar morphology were obtained in the case of GaS as well. The deposits contained wall structures with smooth curved surfaces as revealed by the SEM images presented in Fig. 24a. The XRD pattern of the sample could be indexed on the hexagonal phase of GaSe. The EDAX spectrum recorded at various locations of the sample confirmed the Ga:Se ratio to be 1:1. TEM images revealed that the walls are transparent, especially at the edges, indicating a thickness of around a few nanometers. The nanowalls are single-crystalline, as established by the HREM images as well as the SAED patterns (Fig. 24b). The lattice spacing observed in the HREM image of 3.229 Å corresponds to the separation between the [100] planes of GaSe in the space group $P6_3/mmc$. In the initial stage, the exfoliated sheets deposited in the cooler end of the tube melt, forming droplets. Flower-like nanostructures form around these droplets (inset in Fig. 24a) and grow with time, forming extended network structures. The Ga_2O_3 nanowalls were obtained by heating GaS and

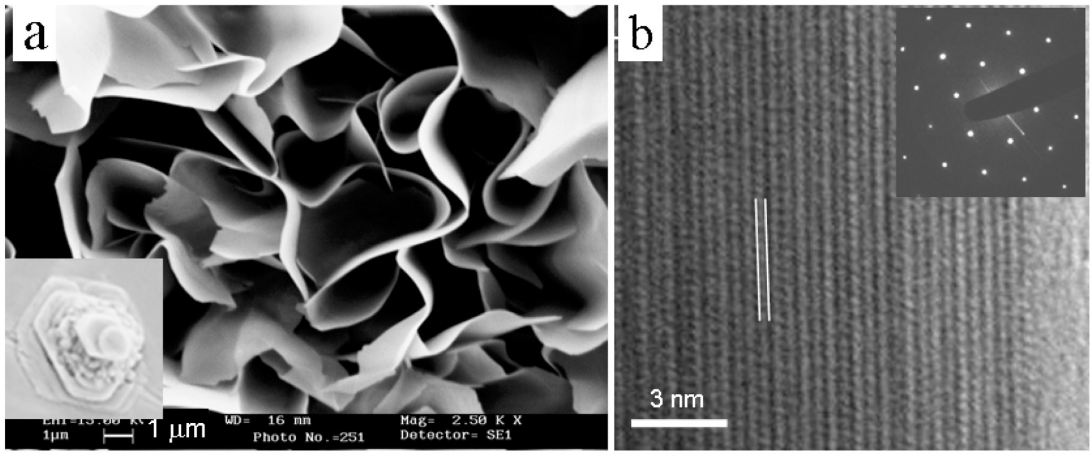

Fig. 24 (a) SEM image of GaSe nanowalls deposited at 400 °C. (b) HREM image of a nanowall. The separation between the lattice planes (3.229 Å ≈ d_{100}) is shown in the image. Inset shows the SAED pattern.

GaSe nanowalls in air at 550 °C. On the other hand, heating the GaS and GaSe nanowalls in NH_3, GaN nanowalls were obtained.

Single-crystalline films of metal chalcogenides

The use of the organic–aqueous interface to prepare nanocrystalline films was described earlier. While many metals and metal sulfides yield films of nanocrystal assemblies, extended ultra-thin single-crystalline films are obtained in the case of CuS [85]. Single-crystalline films of CuSe, ZnS, PbS, $Cu(OH)_2$, and ZnO have also been prepared similarly [32]. To prepare a CuS film, 75 ml of 0.12 mM $Cu(cup)_2$ solution in toluene was slowly added to 75 ml of 0.5 mM Na_2S taken in a crystallization dish (10 cm diameter). An excess of Na_2S was required in order to prevent the formation of Cu_2S. The interface gradually turns green, and the CuS film formed at the interface after 12 h, while the two liquid phases remained colorless. The film grows slowly with time, first appearing as green islands at the interface (in the initial 1–2 h) and slowly covering the entire interface. Figure 25a shows a typical low-magnification TEM image of the CuS film mentioned above. As can be seen, the film is fairly continuous and extends over a wide area. Small fragments on the edges of the film are also seen as the film breaks while lifting from the interface. The single-crystalline and essentially defect-free nature of the film can be inferred from the HREM image and the SAED pattern in Fig. 25b. The lattice spacing of 2.7 Å in the HREM image corresponds to the separation between (006) planes of the hexagonal CuS phase. The diffraction spots could be indexed on the basis of the hexagonal structure ($P6_3/mmc$, a = 3.792 Å and c = 16.34 Å). The thickness of the film was estimated to be ~50 nm from AFM and ellipsometric studies. Thicker films could be formed using higher concentration of reactants. The films prepared at higher temperatures are, however, less continuous and form flakes and rods. An HREM image of such a rod obtained at 70 °C is shown in Fig. 25c. Nanorods and nanocrystals of various sizes and shapes were obtained upon sonication the CuS films. Figures 25d and 25e show TEM images of some such nanocrystals.

Extended single-crystalline films of ZnS are obtained by this method starting with $Zn(cup)_2$ and Na_2S [86]. A TEM image of the film is given in Fig. 26a. The UV/vis absorption spectrum of a ZnS film obtained by reacting 5 mg of $Zn(cup)_2$ in 50 ml of toluene at ~30 °C for 12 h shows an absorption band at ~320 nm (Fig. 26b(i)), close to that of bulk ZnS [87]. The PL spectrum of the ZnS film in Fig. 26b(ii) displays a broad emission band centered at ~425 nm due to the presence of sulfur vacan-

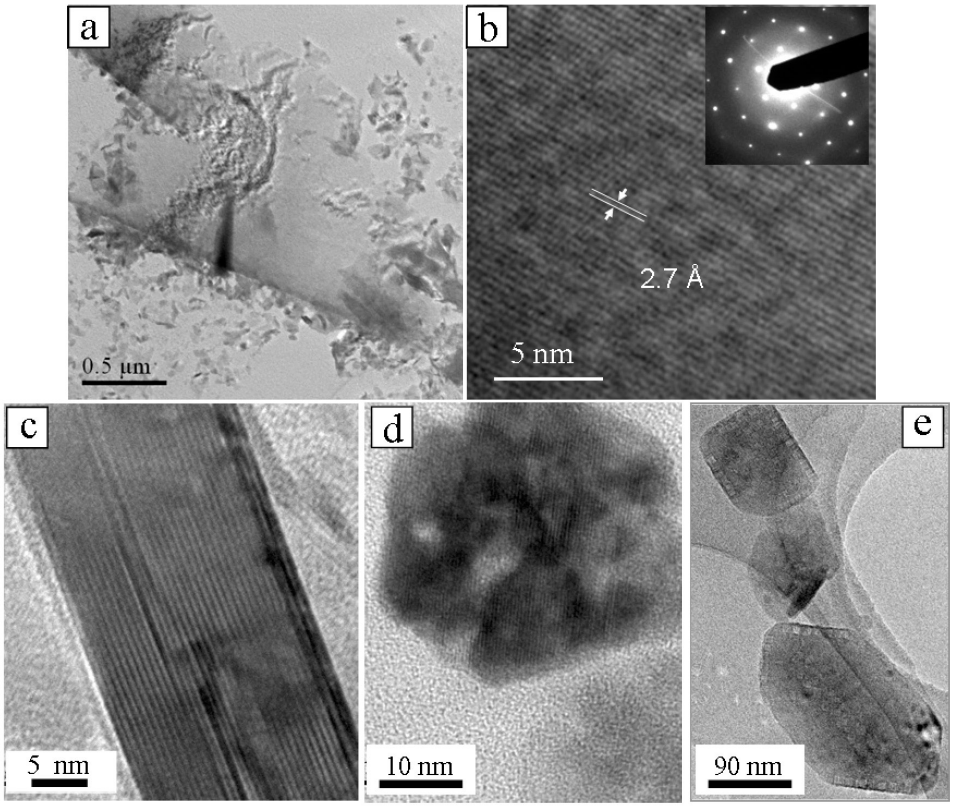

Fig. 25 (a) TEM images of an ultra-thin film of CuS obtained at the toluene–water interface. (b) HREM image of the film. Inset shows the corresponding SAED pattern. (c) HREM image of a rod-like fragment obtained at 70 °C. (d) Hexagonal CuS nanocrystals obtained by sonication of the film obtained with 2 mg of $Cu(cup)_2$ and (e) the nanocrystals obtained using 1 mg of $Cu(cup)_2$.

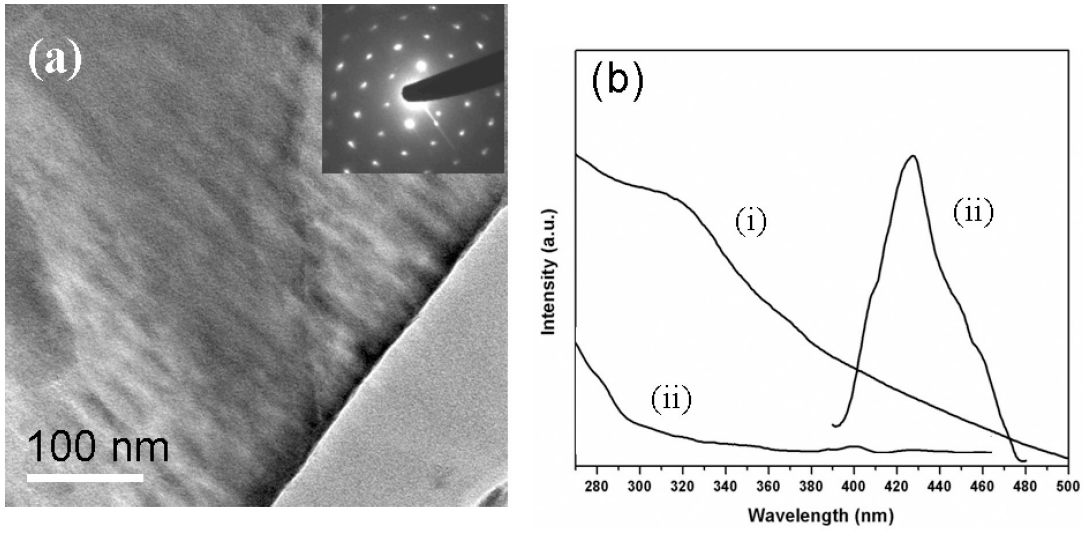

Fig. 26 (a) TEM image of a ZnS film obtained by the reaction of 5 mg of $Zn(cup)_2$ in 50 ml of toluene with 5.7 mg of Na_2S in 30 ml of water at 30 °C.

cies in the ZnS lattice. A blue-shift of the absorption band to 285 nm was observed when the reaction time was restricted to 1 h (Fig. 26 b(iii)), suggesting a thin, incompletely formed film. Unlike chemical methods such as the LB technique where non-single-crystalline films are obtained by assembling nanocrystals or CVD and related techniques where stringent conditions as well as substrates are required, the interface method is simple and can be extended to a variety of materials.

CONCLUSIONS

The various case studies discussed in the previous sections should demonstrate the use of chemical methods, in particular soft chemical routes, for the preparation of nanocrystals and nanowires of a variety of inorganic materials. Many of the materials cannot be prepared by conventional ceramic methods or physical methods. Equally important is the progress made toward inorganic nanotubes. It is noteworthy that the chemical methods are generally simple and cost-effective. Furthermore, the nanostructures are generally single-crystalline. The synthesis of nanofilms by the liquid–liquid interface method is especially important, since the method affords excellent ultra-thin (often single-crystalline) films which are substrate free. In addition, chemical routes give rise to novel material, many of which are metastable.

REFERENCES

1. G. Schimd. *Chem. Rev*. **92**, 1709 (1992).
2. J. H. Fendler (Ed.). *Nanoparticles and Nanostructured Films*, Wiley-VCH, Weinheim (1998).
3. C. N. R. Rao, A. Mueller, A. K. Cheetham (Eds.). *The Chemistry of Nanomaterials*, p. 51, Wiley-VCH, Weinheim (2004).
4. C. N. R. Rao, A. Govindaraj. *Nanotubes and Nanowires*, Royal Society of Chemistry, London (2005).
5. M. Remskar. *Adv. Mater.* **16**, 1497 (2004).
6. K. K. Schuegraf. *Handbook of Thin-film Deposition Processes and Techniques: Principles, Methods, Equipment and Applications*, Noyes Publishing, Park Ridge, NJ (1988).
7. Y. Wu, B. Yang, B. Zong, H. Sun, Z. Shen, Y. Feng. *J. Mater. Chem.* **14**, 469 (2004).
8. C. N. R. Rao, G. U. Kulkarni, P. J. Thomas, P. P. Edwards. *Chem. Soc. Rev.* **29**, 27 (2000).
9. M. Brust, M. Walker, D. Bethell, D. J. Schiffrin, R. Whyman. *Chem. Commun.* 801 (1994).
10. K. V. Sarathy, G. Raina, R. T. Yadav, G. U. Kulkarni, C. N. R. Rao. *J. Phys. Chem. B* **101**, 9876 (1997).
11. K. V. Sarathy, G. U. Kulkarni, C. N. R. Rao. *Chem. Commun.* 537 (1997).
12. P. J. Thomas, G. U. Kulkarni, C. N. R. Rao. *J. Phys. Chem. B* **104**, 8138 (2000).
13. T. Teranishi, M. Miyake. *Chem. Mater.* **10**, 594 (1998).
14. C. N. R. Rao, B. Raveau. *Transition Metal Oxides*, 2nd ed., Wiley-VCH, Weinheim (1995).
15. G. A. El-Shobaky, M. M. Selim, I. F. Hewaidy. *Surf. Technol.* **10**, 55 (1980).
16. M. Ghosh, E. V. Sampathkumaran, C. N. R. Rao. *Chem. Mater.* **17**, 2348 (2005).
17. R. Seshadri. In *The Chemistry of Nanomaterials*, C. N. R. Rao, A. Mueller, A. K. Cheetham (Eds.), p. 94, Wiley-VCH, Weinheim (2004).
18. K. Biswas, C. N. R. Rao. *J. Phys. Chem. B* **110**, 842 (2006).
19. R. E. Kardzhieva, A. A. Andreev. *Z. Neorg. Khimii* **22**, 2007 (1977).
20. S. Link, M. A. El-Sayed. *Int. Rev. Phys. Chem.* **19**, 409 (2000).
21. A. Ferretti, D. B. Rogers, J. B. Goodenough. *J. Phys. Chem. Solids* **26**, 2007 (1965).
22. R. K. Quinn, P. G. Neiswander. *Mater. Res. Bull.* **5**, 329 (1970).
23. U. K. Gautam, R. Seshadri, C. N. R. Rao. *Chem. Phys. Lett.* **375**, 560 (2003).
24. L. Spanhel, H. Haase, H. Weller, A. Henglein. *J. Am. Chem. Soc.* **109**, 5649 (1987).
25. U. K. Gautam, M. Rajamathi, F. Meldrum, P. Morgan, R. Seshadri. *Chem. Commun.* 629 (2001).

26. U. K. Gautam, R. Seshadri. *Mater. Res. Bull.* **39**, 669 (2004).
27. S. Nakamura, G. Fasol. *The Blue Laser Diode*, Springer Verlag, Heidelberg (1997).
28. K. Sardar, C. N. R. Rao. *Adv. Mater.* **16**, 425 (2004).
29. K. Sardar, C. N. R. Rao. *Solid State Sci.* **7**, 217 (2005).
30. K. E. Gonsalves, S. P. Rangarajan, G. Carlson. *Appl. Phys. Lett.* **71**, 2175 (1997).
31. L. Grocholl, J. Wang, E. G. Gillan. *Chem. Mater*. **13**, 4290 (2001).
32. C. N. R. Rao, G. U. Kulkarni, V. V. Agrawal, U. K. Gautam, M. Ghosh, U. Tumkurkar. *J. Colloid Interface Sci.* **289**, 305 (2005).
33. C. J. Kiely, J. Fink, M. Brust, D. Bethell, D. J. Schiffrin. *Nature* **396**, 444 (1998).
34. S. Sun, C. B. Murray, D. Weller, L. Folks, A. Moser. *Science* **287**, 1989 (2000).
35. B. P. Binks, J. H. Clint. *Langmuir* **18**, 1270 (2002).
36. K. R. Patil, D. V. Paranjape, S. D. Sathaye, A. Mitra, S. R. Padalkar, A. B. Mandale. *Mater. Lett.* **46**, 81 (2000).
37. M. Platt, R. A. W. Dryfe, E. P. L. Roberts. *Electrochim. Acta* **49**, 3937 (2004).
38. C. N. R. Rao, G. U. Kulkarni, P. J. Thomas, V. V. Agarwal, P. Saravanan. *Curr. Sci.* **85**, 1041 (2003).
39. C. N. R. Rao, G. U. Kulkarni, P. J. Thomas, V. V. Agarwal, P. Saravanan. *J. Phys. Chem. B* **107**, 7391 (2003).
40. V. V. Agrawal, P. Mahalakshmi, G. U. Kulkarni, C. N. R. Rao. *Langmuir* (ASAP article).
41. U. Kreibig, M. Vollmer. *Optical Properties of Metal Clusters*, p. 25, Springer Verlag, Berlin (1995).
42. U. K. Gautam, M. Ghosh, C. N. R. Rao. *Chem. Phys. Lett.* **381**, 1 (2003).
43. E. Gerlach, P. Grosse. *The Physics of Selenium and Tellurium*, Springer Verlag, Berlin (1979).
44. D. M. Chizhikov, V. P. Shchastlivyi. *Selenium and Selenides*, Collets Publishing, London (1968).
45. Z. Liu, Z. Hu, Q. Xie, B. Yang, J. Wu, Y. Qian. *J. Mater. Chem.* **13**, 159 (2003).
46. U. K. Gautam, M. Nath, C. N. R. Rao. *J. Mater. Chem.* **13**, 2845 (2003).
47. D. L. Klayman, T. S. Griffin. *J. Am. Chem. Soc.* **95**, 197 (1973).
48. U. K. Gautam, C. N. R. Rao. *J. Mater. Chem.* **14**, 2530 (2004).
49. T. T. Albrecht, J. Schotter, G. A. Kästle, N. Emley, T. Shibauchi, L. Krusin-Elbaum, K. Guarini, C. T. Black, M. T. Tuominen, T. P. Russell. *Science* **290**, 2126 (2000).
50. J. Bao, C. Tie, Z. Xu, Q. Zhou, D. Shen, Q. Ma. *Adv. Mater.* **13**, 1631 (2001).
51. L. Sun, P. C. Searson, C. L. Chein. *Appl. Phys. Lett.***79**, 4429 (2001).
52. C. N. R. Rao, K. P. R. Pisharody. *Prog. Solid State Chem.* **10**, 207 (1976).
53. M. Nath, A. Chaudhury, A. Kundu, C. N. R. Rao. *Adv. Mater.* **15**, 2098 (2003).
54. M. Nath, A. Chaudhury, C. N. R. Rao. *Chem. Commun.* 2698 (2004).
55. Y. Qiu, L. Gao. *J. Am. Ceram. Soc.* **87**, 352 (2004).
56. C. N. R. Rao, A. Govindaraj, F. L. Deepak, N. A. Gunari, M. Nath. *Appl. Phys. Lett.* **78**, 1853 (2001).
57. F. L. Deepak, A. Govindaraj, C. N. R. Rao. *J. Nanosci. Nanotechnol.* **2**, 417 (2002).
58. Y. Ono, K. Nakashima, M. Sano, Y. Kanekiyo, K. Inoue, J. Hojo, S. Shinkai. *Chem. Commun.* 1477 (1998).
59. G. Gundiah, S. Mukhopadhyay, U. Tumkurkar, A. Govindaraj, U. Maitrab, C. N. R. Rao. *J. Mater. Chem.* **13**, 2118 (2003).
60. U. Maitra, S. Mukhopadhyay, A. Sarkar, P. Rao, S. S. Indi. *Angew. Chem., Int. Ed*. **40**, 2281 (2001).
61. S. R. C. Vivekchand, G. Gundiah, A. Govindaraj, C. N. R. Rao. *Adv. Mater.* **16**, 1842 (2004).
62. B. Ita, P. Murugavel, V. Ponnambalam, A. R. Raju. *Proc. Indian Acad. Sci.* **115**, 519 (2003).
63. P. Murugavel, M. Kalaiselvam, A. R. Raju, C. N. R. Rao. *J. Mater. Chem.* **7**, 1433 (1997).
64. P. Murugavel, M. Kalaiselvam, M. K. Renganathan, A. R. Raju. *Mater. Chem. Phys.* **53**, 247 (1998).

65. M. Langlet, J. C. Joubort. In *Chemistry of Advanced Materials*, C. N. R. Rao (Ed.), p. 55, Blackwell Scientific, Oxford (1993).
66. R. Sen, A. Govindaraj, C. N. R. Rao. *Chem. Phys. Lett.* **267**, 276 (1997).
67. S. R. C. Vivekchand, L. M. Cele, F. L. Deepak, A. R. Raju, A. Govindaraj. *Chem. Phys. Lett.* **386**, 313 (2004).
68. S. Nakamura, S. F. Chichibu. *Introduction to Nitride Semiconductor Blue Lasers and Light Emitting Diodes*, p. 8, Taylor and Francis, Philadelphia (2000).
69. H. Morkoc, S. N. Mohammad. *Science* **267**, 51 (1995).
70. X. Chen, J. Li, Y. Cao, Y. Lan, H. Li, M. He, C. Wang, Z. Zhang, Z. Qiao. *Adv. Mater.* **12**, 1432 (2000).
71. C. C. Chen, C. C. Yeh, C. H. Chen, M. Y. Yu, H. L. Liu, J. J. Wu, K. H. Chen, L. C. Chen, J. Y. Peng, Y. F. Chen. *J. Am. Chem. Soc.* **123**, 2791 (2001).
72. J. Zhang, L. Zhang, X. Peng, X. Wang. *J. Mater. Chem.* **12**, 802 (2002).
73. K. Sardar, F. L. Deepak, A. Govindaraj, M. M. Seikh, C. N. R. Rao. *Small* **1**, 91 (2005).
74. D. D. Ma, C. S. Lee, Y. Lifshitz, S. T. Lee. *Appl. Phys. Lett.* **81**, 3233 (2002).
75. X. T. Zhou, T. K. Sham, Y. Y. Shan, X. F. Duan, S. T. Lee, R. A. Rosenberg. *J. Appl. Phys.* **97**, 104315 (2005).
76. Y. Feldman, E. Wasserman, D. J. Srolovitz, R. Tenne. *Science* **267**, 222 (1995).
77. R. Tenne, C. N. R. Rao. *Philos. Trans. R. Soc. London, Ser. A* **362**, 2099 (2004).
78. M. Nath, C. N. R. Rao. *J. Chem. Soc., Dalton Trans.* 1 (2003).
79. M. Nath, C. N. R. Rao, R. P. Biro, A. A. Yaron, R. Tenne. *Chem. Mater.* **16**, 2238 (2004).
80. M. Cote, M. Cohen, D. Chadi. *J. Phys. Rev. B* **58**, 4277 (1998).
81. T. Kohler, T. Frauenheim, Z. Hajnal, G. Seifert. *Phys. Rev. B* **69**, 193403 (2004).
82. U. K. Gautam, S. R. C. Vivekchand, A. Govindaraj, G. U. Kulkarni, N. R. Selvi, C. N. R. Rao. *J. Am. Chem. Soc.* **127**, 3658 (2005).
83. H. T. Na, J. Li, M. K. Smith, P. Nguyen, A. Cassell, J. Han, M. Meyyappan. *Science* **300**, 1249 (2003).
84. U. K. Gautam, S. R. C. Vivekchand, A. Govindaraj, C. N. R. Rao. *Chem. Commun.* **31**, 3995 (2005).
85. U. K. Gautam, M. Ghosh, C. N. R. Rao. *Langmuir* **20**, 10775 (2004).
86. K. P. Kalyanikutty, U. K. Gautam, C. N. R. Rao. *Solid State Sci.* **8**, 296 (2006).
87. J. Nanda, S. Sapra, D. D. Sarma, N. Chandrasekharan, G. Hodes. *Chem. Mater.* **12**, 1018 (2002).